Modelling predicts a molecule-rich disc around the AGB star L₂ Puppis

M. Van de Sande [1,2]★ C. Walsh,[1] T. Danilovich [3,4,5], F. De Ceuster [5] and T. Ceulemans [5]

[1]*School of Physics and Astronomy, University of Leeds, Leeds LS2 9JT, UK*
[2]*Leiden Observatory, Leiden University, P.O. Box 9513, NL-2300 RA Leiden, the Netherlands*
[3]*School of Physics and Astronomy, Monash University, Wellington Road, Clayton 3800, Victoria, Australia*
[4]*ARC Centre of Excellence for All Sky Astrophysics in 3 Dimensions (ASTRO 3D), Clayton 3800, Victoria, Australia*
[5]*Institute of Astronomy, KU Leuven, Celestijnenlaan 200D, B-3001 Leuven, Belgium*

ABSTRACT

The nearby oxygen-rich AGB star L_2 Pup hosts a well-studied nearly edge-on disc. To date, discs around AGB stars have not been chemically studied in detail. By combining a parametrization commonly used for protoplanetary discs and archival ALMA observations, we retrieved an updated density and temperature structure of this disc. This physical model was then used as input to the first chemical model of an AGB disc. The model shows that the physical structure of the disc has a large impact on its chemistry, with certain species showing large changes in column density relative to a radial outflow, indicating that chemistry could be used as a tracer of discs that cannot be directly imaged. Despite its oxygen-rich nature, the daughter species formed within the disc are surprisingly carbon-rich. Two chemical regimes can be distinguished: cosmic-ray induced chemistry in the midplane and photochemistry induced by the interstellar radiation field in the outer regions. Certain complex organic molecules are formed in the midplane. This occurs via gas-phase chemistry only, as the disc is too warm for dust-gas chemistry. The photochemistry in the outer regions leads to the efficient formation of (long) carbon-chains. The predictions of the model allow us to tentatively put the disc's age $\lesssim 10^5$ yr. Additional observations are necessary to better constrain the physical structure of L_2 Pup's disc and are essential to test the predictions made by the chemical model. Our exploratory work paves the way for a more general study of the chemistry of AGB discs.

Key words: astrochemistry – molecular processes – radiative transfer – stars: AGB and post-AGB – circumstellar matter – stars: individual: HD 56096, L_2 Puppis.

1 INTRODUCTION

The asymptotic giant branch (AGB) phase near the end of the lives of stars with an initial mass up to 8 $M_\odot$ is characterized by vigorous mass-loss. AGB stars lose their outer layers via a stellar wind or outflow at a rate between 10^{-8} and 10^{-4} $M_\odot$ yr^{-1}, creating an expanding circumstellar envelope (CSE; Habing & Olofsson 2003; Höfner & Olofsson 2018). CSEs are rich astrochemical environments, with close to 100 different molecules and some 15 types of newly formed dust grains detected so far (Decin 2021). Spherically symmetric outflows appear to be the exception rather than the rule. Asymmetrical structures are ubiquitously observed, ranging from small-scale asymmetries, such as density-enhanced clumps (e.g. Leão et al. 2006; Khouri et al. 2016; Velilla-Prieto et al. 2023), to large-scale structures, such as spirals (e.g. Mauron & Huggins 2006; Maercker et al. 2012) and discs (e.g. Kervella et al. 2016). These large-scale structures are thought to be caused by binary interaction with (sub)stellar companions. Circumbinary discs are expected around younger, lower mass-loss rate AGB stars, evolving into spirals as the mass-loss rate increases and the companion's orbit widens during the AGB phase (Decin et al. 2020).

The classic spherically symmetric 1D chemical kinetics model of the CSE is hence applicable to only a minority of outflows. The effects of the UV field of a stellar companion and a clumpy substructure on the chemistry throughout the outflow have been included in chemical models of the CSE (Van de Sande et al. 2018; Van de Sande & Millar 2022; Van de Sande, Walsh & Millar 2023). These models show that chemistry can be used to unveil a hidden stellar companion (Siebert et al. 2022) and retrieve its orbital properties (Danilovich et al. 2024). The influence of large-scale density structures on the CSE's chemistry requires specialized chemical models. So far, models have been developed for the density-enhanced shells in the outflow of IRC+10216 (Brown & Millar 2003; Cordiner & Millar 2009; Agúndez et al. 2017), but no general models applicable to a larger set of AGB stars exist. The chemistry of discs around AGB stars has not been studied in detail.

The best-studied AGB disc is that around the oxygen-rich AGB star L_2 Pup, the second-closest AGB star at a distance of 64 pc (van Leeuwen 2007). Optical and infrared observations have shown the clear presence of an almost edge-on compact dusty disc with an inner dust rim at 6 au, spanning to around 15 au. Loops and plumes extending above the disc have also been identified (Ireland et al. 2004; Kervella et al. 2014, 2015; Lykou et al. 2015; Ohnaka et al. 2015). ALMA observations probed the gaseous disc, which has an inner rim at 2 au, and revealed a tentative planetary companion with

★ E-mail: mvdsande@strw.leidenuniv.nl

a mass of 12 ± 16 M$_J$. This planet is probably not formed within the disc, but is instead rather part of L$_2$ Pup's (first generation) planetary system (Chen et al. 2016; Kervella et al. 2016). The physical structure of the disc has been proposed to be similar to that of protoplanetary discs (PPDs), albeit with a higher temperature in the midplane as it is assembled from warm stellar outflow material (Homan et al. 2017).

In this paper, we develop a 2D chemical model of L$_2$ Pup's disc: the first such model of a disc around an AGB star. This exploratory work probes the unique astrochemical regime of a hot and dense disc, irradiated by the interstellar radiation field. By determining the effects of the physical disc structure on the chemistry around L$_2$ Pup, we can identify the chemical differences with a spherically symmetric O-rich outflow and establish whether the parent species are redistributed into different carriers. Such differences can be used as chemical tracers of discs that are not as easily resolved as the close-by L$_2$ Pup. Additionally, the evolution of the disc's chemical structure over time can be used to determine the age of the disc.

In Section 2, we use archival ALMA data to retrieve the disc's density and temperature structure using a parametric model commonly used for PPDs. This physical structure is then used as input to the chemical model in Section 3, where we also show the chemical modelling results. The physical and chemical modelling results are discussed in Section 4, followed by our conclusions in Section 5.

2 PHYSICAL MODEL

L$_2$ Pup was observed by ALMA during Cycle 3 for project 2015.1.00141.S (PI Pierre Kervella) in 2015 November. The reduction of the Band 7 observations is described in Kervella et al. (2016), and we use that data set in this work. The resulting data have an angular resolution better than 15 mas and a maximum resolvable scale of 200 mas. The $J = 3 - 2$ lines of ^{12}CO and ^{13}CO from the data set are presented in Homan et al. (2017). The data cubes have a spectral resolution of 0.22 km s^{-1} and an rms noise level of 2.5 and 2.6 mJy beam^{-1}, respectively. The channel maps of the lines are presented here in Figs A1 and A2 in Appendix A, now with beam information.

Homan et al. (2017) derived a physical model of L$_2$ Pup's disc from the ^{12}CO and ^{13}CO $J = 3 - 2$ lines. The model from that work, although provided by the first author, was unable to be reproduced. Given the similarity of the disc to PPDs, we opted to remodel the data using a parametric model commonly used for PPDs.

The parametric model is described in Section 2.1. Section 2.2 describes the 3D line radiative transfer code used, MAGRITTE. The parameter space explored is laid out in Section 2.3, the retrieved physical structure of the disc is presented in Section 2.4.

2.1 Parametric model of a protoplanetary disc

We use the parametrization of Williams & Best (2014), which assumes a disc surface density profile based on the solution for an axisymmetric, steady-state viscous accretion disc in hydrostatic equilibrium (e.g. Lynden-Bell & Pringle 1974; Hartmann et al. 1998). The surface density of the disc is described by

$$\Sigma(r) = \Sigma_0 \left(\frac{r}{r_0}\right)^{-\gamma} \exp\left(-\left(\frac{r}{r_0}\right)^{2-\gamma}\right), \qquad (1)$$

where r_0 is a disc reference radius and γ describes the radial dependence. Σ_0 gives the global normalization to the gas mass at

r_0, written as

$$\Sigma_0 = (2 - \gamma) \frac{M_{\text{gas}}}{2\pi r_0^2} \exp\left(\frac{r_{\text{in}}}{r_0}\right)^{2-\gamma}, \qquad (2)$$

with M_{gas} the disc's total gas mass and r_{in} its inner radius. Assuming hydrostatic vertical balance in the disc, the density structure of the disc is described by

$$\rho(r, z) = \frac{\Sigma(r)}{H_p(r)\sqrt{2\pi}} \exp\left(-\frac{z^2}{2H_p(r)^2}\right), \qquad (3)$$

with H_p the pressure scale height derived from the midplane temperature. This scale height is given by the ratio between the speed of sound, c_s, and the Keplerian angular frequency Ω_K, or,

$$H_p = \frac{c_s}{\Omega_K} = \sqrt{\frac{k_B \, T_{\text{mid}}(r) \, r^3}{G \, M_* \, \mu m_H}}. \qquad (4)$$

Here, M_* is the stellar mass, k_B is the Boltzmann constant, G the gravitational constant, m_H the mass of the hydrogen atom, and μ the mean molecular mass.

The midplane temperature profile is parametrized by a power law,

$$T_{\text{mid}}(r) = T_{\text{mid},1} \left(\frac{r}{1\text{au}}\right)^{-q}, \qquad (5)$$

with $T_{\text{mid},1}$ the temperature at 1 au and q the power-law exponent. Similarly, the atmospheric temperature surrounding the disc is parametrized by

$$T_{\text{atm}}(r) = T_* \left(\frac{r}{1\text{au}}\right)^{-\epsilon}, \qquad (6)$$

with T_* the stellar temperature and ϵ the power-law exponent. The vertical temperature profile connects equations (5) and (6) by a sine function:

$$T(r, z) = \begin{cases} T_{\text{mid}} + (T_{\text{atm}} - T_{\text{mid}}) \left[\sin\left(\frac{\pi z}{2z_q}\right)\right]^{2\delta} & \text{if } z < z_q \\ T_{\text{atm}} & \text{if } z \geq z_q \end{cases}, \qquad (7)$$

where δ describes the steepness of the temperature profile and z_q describes the height at which the disc reaches the atmospheric value. Following Williams & Best (2014), we fix $\delta = 2$ and $z_q = 4H_p(r)$.

For a given stellar mass, the physical structure of the disc is described by eight parameters: four for the density profile, $\{\gamma, r_{\text{in}}, r_0, M_{\text{gas}}\}$, and four for the temperature profile, $\{T_{\text{mid},1}, T_{\text{atm},1}, q, \epsilon\}$.

2.2 MAGRITTE: 3D line radiative transfer

MAGRITTE[1] is an open-source 3D non-LTE line radiative transfer code, mainly used for creating synthetic spectral line observations (De Ceuster et al. 2020a, b, 2022). We initialize the MAGRITTE model by defining the model on a uniform $60 \times 60 \times 30$ au grid. For each point, we define the temperature, velocity, turbulent velocity, H2 density, and CO density. The grid is then resampled to speed up computation by limiting the allowed variation of the density, which we evaluated at the uniform grid positions (Ceulemans et al., in preparation). After model setup, the radiation field is computed assuming non-LTE by taking into account the first seven rotational CO lines. In this way, the energetic state of the CO gas is determined self-consistently. Afterwards, we create spectral line images for the ^{12}CO and ^{13}CO $J = 3 - 2$ lines.

---

[1]Available at https://github.com/Magritte-code/Magritte, we used version 0.3.2.

Table 1. The physical disc model for L$_2$ Pup that best reproduces the data following the parametrization of Williams & Best (2014). The top parameters were fixed based on previous observations. The bottom parameters were obtained from modelling the ^{12}CO and ^{13}CO $J = 3 - 2$ data. Their ranges are described in Section 2.3.

Atmospheric temperature, $T_{\mathrm{atm},1}$	2800 K	(1)
Exponent power law $T_{\mathrm{atm}}(r)$, ϵ	0.65	(2)
Inner radius of the disk, r_{in}	2 au	(2)
Velocity profile up to 6 au	Keplerian	(2)
Velocity profile beyond 6 au	sub-Keplerian, $\propto r^{0.853}$	(2)
Turbulent velocity	0.5 km s^{-1}	(3)
^{12}CO abundance	1×10^{-4} w.r.t. H2	(3)
Total gas mass of the disc, M_{gas}	2.5×10^{-4} M$_\odot$	(4)
Stellar mass, M_*	$0.659 \times$ M$_\odot$	(2)
Midplane temperature, $T_{\mathrm{mid},1}$	900 K	–
Power-law exponent $T_{\mathrm{mid}}(r)$, q	0.2	–
Characteristic disc radius, r_0	6 au	–
Power-law exponent surface density $\Sigma(r)$, γ	−1.0	–
^{13}CO abundance	2×10^{-5} w.r.t. H2	–

Note. References. (1) Danilovich et al. (2015); (2) Kervella et al. (2016); (3) Homan et al. (2017); (4) Kervella et al. (2015).

2.3 Parameter space of the physical model

Table 1 shows the parameters of the physical model along with the values which best reproduce the integrated emission profiles. Based on previous observations, we fixed the inner radius of the disc, velocity profile, temperature profile of the disc's atmosphere, the fractional abundance of ^{12}CO, and the stellar and disc mass. These parameters are listed in the top rows of Table 1. The stellar radius is fixed at 1 au. The inner radius of the disc, r_{in}, is fixed at 2 au (Kervella et al. 2016). The velocity profile is assumed to be Keplerian from the inner radius out to the inner rim of the dusty disc at 6 au. Beyond 6 au, the velocity profile is sub-Keplerian with a power-law exponent of 0.853 (Kervella et al. 2016). The turbulent velocity is fixed to 0.5 km s^{-1} (Homan et al. 2017). The temperature profile of the atmosphere is fixed at $T_{\mathrm{atm},1} = 2800$ K with a power-law exponent of 0.65 (Danilovich et al. 2015). The fractional abundance of ^{12}CO was taken to be 1×10^{-4} with respect to H2 (Homan et al. 2017). The total gas mass of the disc, M_{gas}, is fixed at 2.5×10^{-4} M$_\odot$ following Kervella et al. (2015) and assuming a dust-to-gas mass ratio of 0.01. The stellar mass, M_*, is fixed to $0.659 \times$ M$_\odot$, as derived by Kervella et al. (2016).

The other parameters were allowed to vary and are listed in the bottom rows of Table 1. Their starting points were based on the model of Homan et al. (2017). The midplane temperature, $T_{\mathrm{mid},1}$, was varied in increments of 100 K, the power-law of the midplane temperature, q, in increments of 0.05, the characteristic disc radius, r_0, in increments of 1 au, the parameter determining the surface density (equation 1), γ, in increments of 0.5, and the ^{13}CO abundance in increments of 1×10^{-5} w.r.t. H2.

2.4 Physical structure of the disc

The model calculation was constrained by comparing slices along the disc midplane through the moment 0 (integrated intensity) maps of the observed lines. The moment 0 maps are presented in Kervella et al. (2016) (their figs A1 and B1). The slices were chosen so that they go through the emission peaks in the East and West sides of the disc as the disc's position angle is not zero. We choose to use this metric as a radial slice along the major axis of the disc will capture well the radial behaviour of the emission without any complication that may

arise from deprojection of the emission from this highly inclined disc. The slice through the moment 0 map of ^{12}CO is centred on (07$^{\mathrm{h}}$13$^{\mathrm{m}}$32$^{\mathrm{s}}$.477, -44°38′17″.845) at an angle of 9.53°, that through the ^{13}CO moment 0 map is centred on (07$^{\mathrm{h}}$13$^{\mathrm{m}}$32$^{\mathrm{s}}$.475, -44°38′17″.843) at an angle of 16.0°. The slices are different as the ^{12}CO and ^{13}CO probe different layers within the disc.

We first modelled the ^{12}CO line by reproducing the slice through its moment 0 map. Good models were determined by minimizing the chi-squared value of the fit to the slice. For these models, we then calculated the corresponding ^{13}CO model, varying the ^{13}CO abundance as an additional parameter while keeping the others fixed and calculated the chi-squared value of the fit to the slice through the ^{13}CO moment 0 map. The ^{12}CO/^{13}CO ratio is fixed throughout the disc.

Our best-fitting model provides the best reproduction of the ^{12}CO moment 0 slice, with a chi-squared value of 3.92. A ^{13}CO abundance of 2×10^{-5} results in the fourth-best fit in our sampled parameter space to the ^{13}CO moment 0 slice, with $\chi^2 = 1.76$. A larger ^{13}CO abundance of 3×10^{-5} results in the third-best model, with $\chi^2 = 1.74$. However, this would yield a ^{12}CO/^{13}CO ratio of 3.33. Since this ratio is lower than expected from observations (Ramstedt et al. 2014) and the improvement to reproducing the observations is marginal, we chose the model with a ^{13}CO abundance of 2×10^{-5} as our best model. Note that the model that best reproduces the ^{13}CO moment 0 slice, with the lowest chi-squared value of 1.65, corresponds to the fourth-best model to the ^{12}CO moment 0 slice, with $\chi^2 = 4.19$.

Together with a visual inspection of the moment 0 maps, channel maps, and line profiles, we chose the best-fitting model to the ^{12}CO moment 0 slice with a ^{13}CO abundance of 2×10^{-5} as our final model. Its parameters are listed in Table 1. Fig. 1 shows the slices through the moment 0 maps of the ^{12}CO and ^{13}CO $J = 3 - 2$ lines along with the MAGRITTE model results. The negative flux in at the centre of the observed lines is due to line absorption by the molecular gas located in front of the star. The MAGRITTE model's moment 0 and channel maps are shown in Figs B1, B2, and B3 in Appendix B.

Fig. 2 shows the density and temperature profile of the best-fitting model. We find that L$_2$ Pup's disc has a surface density profile $\Sigma(r) \sim r^{-1}$ and an r_0 of 6 au. This radius corresponds to the radius where the disc's velocity profile changes from Keplerian to sub-Keplerian (Kervella et al. 2016) and where the surface density steepens significantly from a power law (Williams & Cieza 2011). Its midplane is warm with $T_{\mathrm{mid},1} = 900$ K, and has a shallow temperature profile characterized by $q = 0.2$. The ^{13}CO abundance w.r.t. H2 is 2×10^{-5}, yielding a ^{12}CO/^{13}CO ratio of 5.

3 CHEMICAL MODEL

The disc chemical model used is the PPD chemical model of Walsh, Nomura & van Dishoeck (2015), which includes the full gas-phase chemical network of the UMIST Database for Astrochemistry (UDfA) RATE12 (McElroy et al. 2013) supplemented with a comprehensive dust-gas and grain-surface chemistry. The RATE12 gas-phase network includes ion–molecule and neutral–neutral reactions, photoionization, and photodissociation (parametrized to the interstellar radiation field), cosmic-ray-ionization, and cosmic-ray-induced photoreactions. We include all these processes by default. To this base network, Walsh et al. (2015) added a suite of three-body association reactions and hot neutral–neutral reactions (those with a large activation barrier) from compilations used in combustion chemistry (e.g. Baulch et al. 2005). Also added were a set of collisional dissociation reactions for all species expected to be
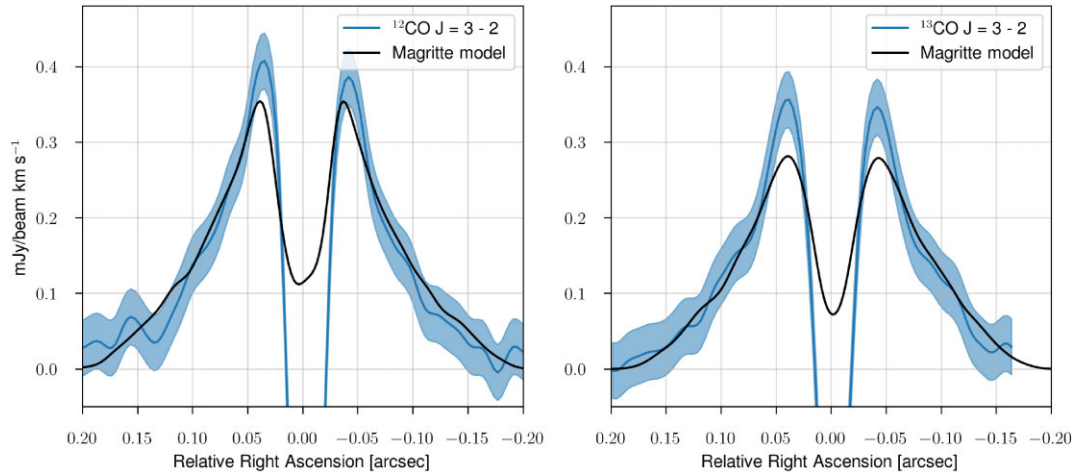
Figure 1. Slice through the moment 0 map of ^{12}CO (left) ^{13}CO $J = 3 - 2$ (right), and along the major axis of the disc (blue) together with the MAGRITTE modelling results (black). The range marked in blue corresponds to the rms error of the moment 0 map of the data. Model parameters are listed in Table 1.
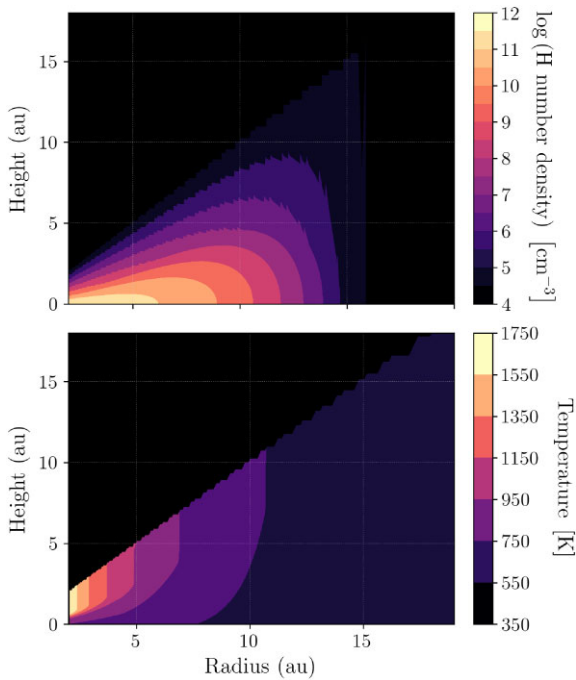
Figure 2. Density (upper panel) and temperature (lower panel) of the MAGRITTE model that best reproduces the observations of L$_2$ Pup's disc. The parameters of the physical model are listed in Table 1.

abundant at the high densities and temperatures expected in inner discs (i.e. mostly saturated molecules and associated radicals).

The protoplanetary disc chemical code also includes a treatment for self- and mutual-shielding of H2, CO, and N2 (see e.g. Heays, Bosman & van Dishoeck 2017). To compute the shielding functions for photodissociation of H2, CO, and N2, we estimate the visual extinction, A_V (mag), at each point in the disc by vertically integrating the H2 column from the disc surface downwards, then scaling the H2 column to A_V using the standard ISM scaling ($0.5 \times (1.59 \times 10^{21}) \times A_V$; Bohlin, Savage & Drake 1978). This is appropriate because the AGB star is very cool ($T_{\rm eff} = 2800 - 3500$ K; Kervella et al. 2014; Danilovich et al. 2015), and the only source of UV radiation is the ISM. We then interpolate the shielding functions provided by Heays

et al. (2017) over A_V and column density, assuming conservative fractional abundances for CO and N2 of 10^{-5} w.r.t. H2. This shielding factor is then added as a pre-factor to the photodissociation rate which is calculated in the usual manner. The chemical model of Walsh et al. (2015) also includes a suite of X-ray reactions and grain surface processes. However, because there is no source of X-rays in this system, X-ray chemistry is effectively inactive and is therefore not included.

The physical model retrieved in Section 2 was used as input to the static chemical model. As there are no observational constraints, we assumed that the dust temperature is equal to the gas temperature. The assumption of thermally coupled dust and gas is reasonable considering the high densities. The dust extinction at each point in the disc was calculated by combining the H2 column densities of the disc and that in the surrounding tenuous outflow in the vertical direction for each point, assuming the ISM relation between A_V and H2 column density. The chemistry is evolved for 10^6 yr, roughly the entire AGB lifetime.

We also calculate a 1D outflow chemical model to compare the predicted disc chemistry with the chemistry in a low-density outflow. The smooth outflow model is the publicly available CSE model of the UDfA RATE22 release (Millar et al. 2024).[2] It describes a spherically symmetric outflow with a constant mass-loss rate and outflow velocity, with a power-law temperature profile. Following Danilovich et al. (2015), we adopt a mass-loss rate of $\dot{M} = 1.4 \times 10^{-8}$ M$_\odot$ yr^{-1}, an expansion velocity of $v_\infty = 2$ km s^{-1}, and a stellar temperature of $T_* = 2800$ K. We use the same exponent for the temperature power law as in the disc physical model, $\epsilon = 0.65$. The density and temperature throughout the outflow is shown in Fig. C1.

Table C1 lists the O-rich parent species and their initial abundances as derived from a range of observations by Agúndez et al. (2020) and augmented by metal abundances (Van de Sande, Walsh & Millar 2021). Note that Kervella et al. (2016) found a sub-solar metallicity of $Z = 0.008$, which could reduce some of our assumed abundances by a factor ~ 2 (Karakas & Lugaro 2016). The parent species are used as input to both chemical models. Therefore, we assume that the material captured during the disc generation phase has the same composition as the inner wind as an approximation of the disc's

[2] https://github.com/MarieVdS/rate22_cse_code
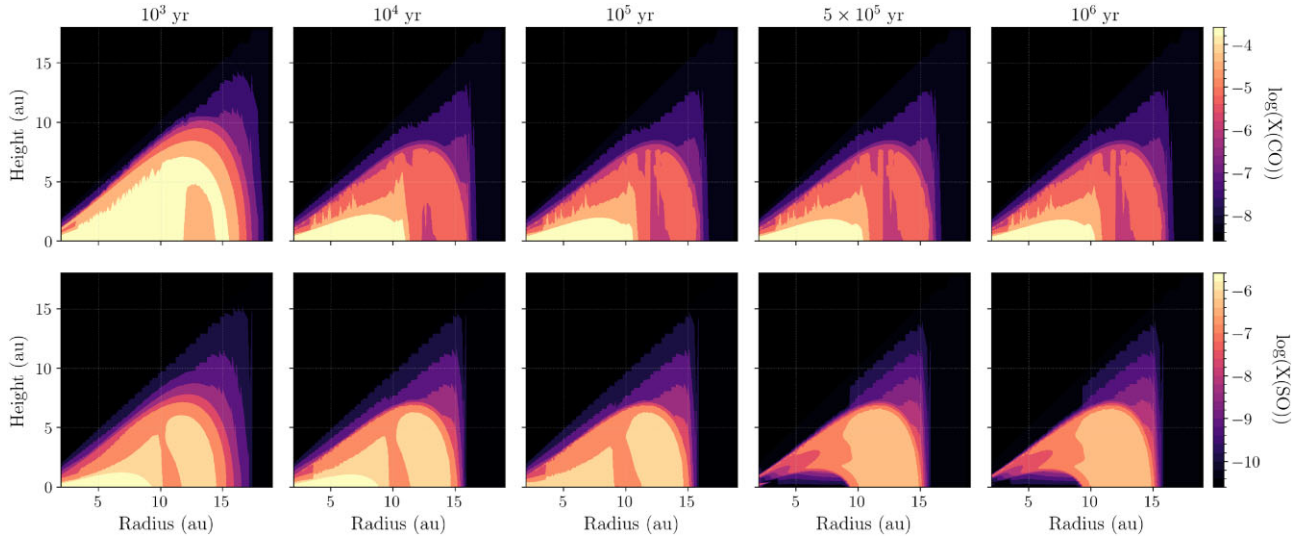
Figure 3. Fractional abundance of CO (top panels) and SO (bottom panels) throughout the disc as predicted by the chemical model. The colour map shows the logarithm of the abundance w.r.t. H2. The different columns show the abundance maps after different times, increasing from left to right.

initial composition. We evolve the chemistry for an initial 10^3 yr as our first snapshot to allow the physical conditions to imprint on the chemistry.

The results of the chemical model are presented in the next sections. We first show the results for the parent species in Section 3.1, followed by the daughters in Section 3.2. The formation of complex organic molecules (COMs) and a C-rich reservoir in the outer regions is shown in Sections 3.3 and 3.4, respectively. All abundances are fractional abundances relative to H2.

3.1 Behaviour of the parent species

Fig. 3 shows the abundance of the parents CO and SO throughout the disc at different time intervals. Their abundance distribution changes over time. The CO abundance decreases in the outer, more tenuous layers due to photodissociation by the interstellar UV radiation field (note that self- and mutual CO self-shielding is included, Section 3). The abundance of SO decreases in the midplane up to a radius of 10 au after 5×10^5 yr, shifting its peak abundance to the outer edge of the disc. This is not due to depletion onto dust as the dust is too warm, but it is caused by reactions with C (liberated predominantly from CO by cosmic rays), which reacts with SO to form CS. SO2 shows similar behaviour (Fig. C2 in Appendix C), where reactions with C lead to the formation of SO. The large C/S abundance ratio of ~ 12 makes these efficient SO and SO2 destruction pathways. The observed emission of SO and SO2 (Kervella et al. 2016) suggests that the disc is likely not older than $\sim 10^5$ yr; this is further discussed in Section 4.3. The abundance profiles of all parents at 10^5 yr are shown in Fig. C3.

The radial extent measured at the midplane of the parents at different times within the disc is shown in Fig. 4, together with the size of their molecular envelopes in the outflow model. These are the radii where the initial abundance has decreased by a factor of e, corresponding to the e-folding radius in the outflow. All parents have a radial extent of ~ 10 au, which is consistent with the disc's density distribution (Fig. 2). This is smaller than the size of their molecular envelope in the outflow, which is larger by a factor of a few (e.g. for H2S or NH3) to two orders of magnitude (for CO and PN). In the disc, the radial extent of most parent species does not change significantly
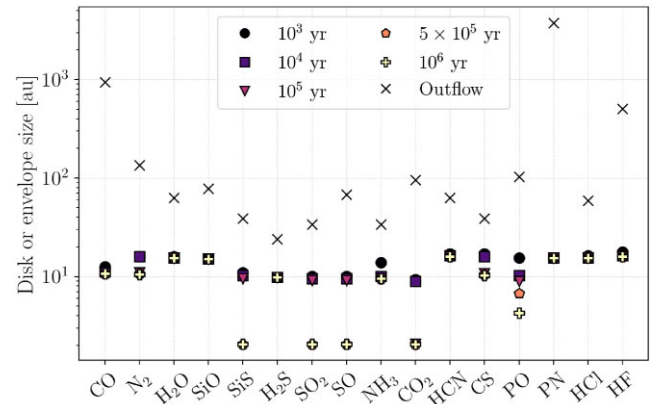
Figure 4. Radial extent of the parent species predicted by the disc and outflow chemical models in au. Their radial extent in the disc measured at the midplane is shown at different times, characterized by different markers and colours. The grey cross shows their extent in a smooth outflow model.

over time. That of the parents SiS, SO2, SO, and CO2 decreases by a factor of $\sim 4 - 5$ over time; that of PO decreases by a factor of ~ 2. For SO2, SO, and CO2, this is due to the abundance decreasing in the midplane followed by photodissociation in the outer layers of the disc. The decrease in radial extent for SiS and PO is purely due to photodissociation, these species do not show a gap in the inner midplane (Fig. C3).

3.2 Behaviour of daughter species

Fig. 5 shows the abundance of the daughters OH, SiC2, CH3CN, and HCOOH throughout the disc at 10^5 yr. The abundance of OH peaks in the outer regions of the disc, with abundances up to $\sim 3 \times 10^{-6}$. This distribution is due to its formation from the photodissociation of the parent H2O and is similar to its behaviour in an outflow, where it forms a molecular shell.

SiC2 is also present in the outer regions of the disc, but its abundance is largest in the inner disc edge where it reaches $\sim 3 \times 10^{-6}$. This is caused by the unique combination of high density, high
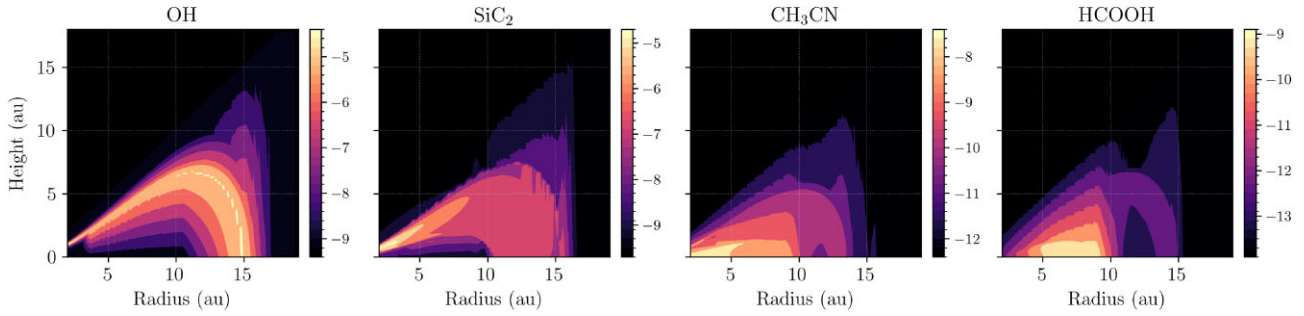
Figure 5. Fractional abundance of the daughters OH, SiC2, CH3CN, and HCOOH throughout the disc as predicted by the chemical model at 10^5 yr. The colour map shows the logarithm of the abundance w.r.t. H2. Note that each colourmap has a different dynamic range.

temperature, and strong UV radiation field in this region. SiC2 is formed by the reaction Si + C2H2, where Si is produced by the photodissociation of the parent SiO. The higher abundance in the inner disc edge is inherited from that of the reactant C2H2 (Fig. C4) and is caused by the temperature dependencies in its formation pathway, which are elaborated on in Section 4.4.4.

CH3CN (methyl cyanide) is not located in the outer edge of the disc, but in the inner disc midplane. Its peak abundance is $\sim 3 \times 10^{-9}$, which is two orders of magnitude larger than its predicted peak abundance in an outflow. This C-bearing molecule is formed via CH3+ and the parent HCN producing CH3CNH+, which then dissociatively recombines by collisions with negatively charged dust grains into CH3CN. CH3+ plays a crucial role in the chemistry of the inner midplane. It is formed via CH4 + He+, where both reactants have a cosmic ray origin, as CH4 is formed by the successive addition of hydrogen to C (liberated by cosmic rays from CO). Section 4.4.1 elaborates on the cosmic-ray induced midplane chemistry.

The abundance of HCOOH (formic acid) is also largest in the midplane. Its peak abundance is $\sim 5 \times 10^{-9}$, three orders of magnitude larger than its peak abundance in an outflow. Its formation is also initiated by cosmic rays: H3+ (a product of cosmic-ray reactions) reacts with the parent CO to form HCO+. Reaction with the parent H2O produces HCOOCH2+ and HCOOH. Unlike CH3CN, its peak abundance is not in the inner regions of the disc but between 5 and 9 au. This is due to the difference in destruction mechanisms: unlike CH3CN, HCOOH is efficiently destroyed by collisional dissociation. The rate of this destruction mechanism increases with density, destroying HCOOH in the dense inner midplane.

3.3 Formation of complex organic molecules

The COMs CH3OH (methanol), CH3CN (vinyl cyanide), CH3NH2 (methylamide), C2H5CN (ethyl cyanide), CH2CHCN (acrylonitrile), HCOOH (formic acid), and HCOOCH3 (methyl formate) are abundantly present in the inner disc and are formed by cosmic-ray induced chemistry in the midplane (Section 4.4.1). Their abundance distribution at 10^5 yr is shown in Fig. 6.

Fig. 7 shows their column density at different times in the disc model, together with their column density in the outflow model. The column density of species in the disc is a disc-averaged column density, calculated via

$$\bar{N} = \frac{2}{\pi r_D^2} \times \sum_{i=0}^{D} 2\pi r_i \Delta r_i N_i, \tag{8}$$

where N_i is the vertical column density within Δr_i and the factor 2 accounts for the symmetry of the model across the midplane. At

10^5 yr, all COMs listed above have a disc-averaged column density larger than 10^{10} cm^{-2}. CH3CN has the largest column density of 1.80×10^{15} cm^{-2}, followed by CH3OH with 3.37×10^{14} cm^{-2} and HCOOH with 1.19×10^{14} cm^{-2}. The column densities are at least five orders of magnitude larger than those predicted by the outflow model. The largest differences are seen for CH3NH2, C2H5CN, CH2CHCN, and HCOOCH3, with a difference of at least 8 orders of magnitude, showing that the chemistry in the disc is favouring the formation of larger saturated complex molecules.

3.4 Carbon-rich reservoir in the outer regions

Carbon-bearing molecules are abundantly formed in the outer regions of the disc. CO and other C-bearing parents are photodissociated by interstellar UV photons, liberating the reactive C atom. Carbon-chains, e.g. C2H2 and HC3N, are abundantly formed in this region (Fig. C4). Longer highly unsaturated carbon chains, such as C10H2, C8H, and HC9N, are also produced. However, the chemical reaction network is geared towards interstellar chemistry and does not include full saturation of these carbon chains. Hence, the predicted abundances of these longer chains are likely overestimated.

We therefore grouped all species with 6 or more C atoms into a 'carbon sink' reservoir. Fig. 8 shows the abundance of this sink particle throughout the disc at different times in its evolution. The total abundance of carbon-bearing species is large in the outer disc, with a maximum abundance of $\sim 3 \times 10^{-5}$. This is remarkably large considering the disc is O-rich. Unlike in the outer regions of an AGB outflow, newly liberated C can readily react and form (long) carbon chains thanks to the higher densities in the disc's outer region.

4 DISCUSSION

The physical structure of the disc has a large influence on the chemistry around L₂ Pup. In Section 4.1, we compare our newly derived physical structure to PPDs and discs around post-AGB stars. We then compare our results to those of Homan et al. (2017) and suggest future observations to better constrain the density and temperature within the disc. This is important, as the predicted chemistry depends on the physical structure. In Section 4.2, we qualitatively compare our predicted abundance profiles to the previous observations of Kervella et al. (2016) as a first-order test of the model. We elaborate on using the predicted SO and SO2 abundance profiles to age the disc at $\sim 10^5$ yr in Section 4.3. Finally, the chemistry within the disc is discussed in Section 4.4, where we examine the surprisingly rich C-rich chemistry in the O-rich disc and suggest molecular tracers of the disc structure.
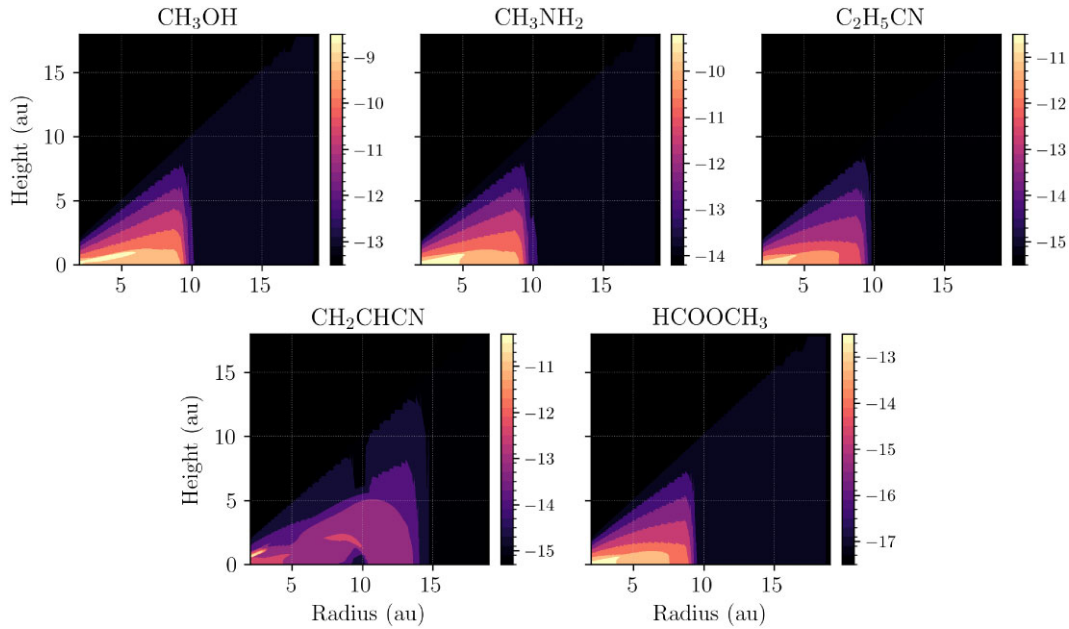
Figure 6. Fractional abundances of complex organic molecules (COMs) formed within the disc as predicted by the chemical model after 10^5 yr. The colour map shows the logarithm of the abundance w.r.t. H2. Note that each colour map has a different dynamic range. The additional COMs CH3CN and HCOOH are shown in Fig. 5.
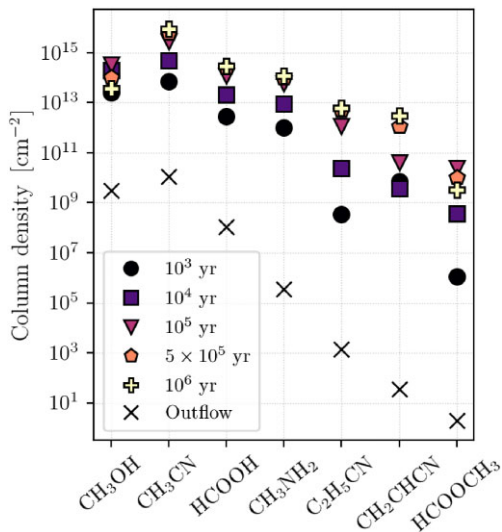
Figure 7. Disc-averaged column densities of COMs produced in the chemical model of the disc at different times, characterized by different markers and colours. The grey cross shows the results from a smooth outflow model.

4.1 Physical structure of the disc

We compare our retrieved physical structure of the disc around L_2 Pup to PPDs and post-AGB discs in Section 4.1.1. A comparison to the previous model of Homan et al. (2017) is made in Section 4.1.2. Since our physical model was retrieved using just two molecular emission lines, we describe the observations needed for a further refinement of the model in Section 4.1.3.

4.1.1 Comparison to PPDs and post-AGB discs

We retrieved that the disc around L_2 Pup has a surface density profile $\Sigma(r) \sim r^{-1}$ and is warm, with a midplane temperature of

900 K and $T_{\mathrm{mid}}(r) \sim r^{-0.2}$. The exponent of the surface density distribution, γ, is on the shallower end of those found for PPDs, for which $\gamma \lesssim -1$ (Andrews 2020). Discs around post-AGB stars have $-3 \leq \gamma \leq -1$, although it is difficult to constrain this value with infrared interferometry alone (Hillen et al. 2014, 2015; Corporaal et al. 2023). Our value of $\gamma = -1$ hence also agrees with post-AGB discs and appears to suggest that the density profile of this disc around an AGB star lies between that of a PPD and post-AGB disc.

The midplane temperature of L_2 Pup's disc is much warmer than in PPDs: $T_{\mathrm{mid},1} = 900$ K compared to $100 - 300$ K for PPDs. The power law is also flatter, with $q = 0.2$ rather than $q = 0.5 - 0.7$ for PPDs (e.g. Andrews et al. 2009; Williams & Best 2014). The temperatures of post-AGB discs lie within $1400 - 3600$ K, which are single blackbody temperatures for the disc as it is, again, difficult to constrain their midplane temperatures using infrared interferometry alone (Kluska et al. 2018; Corporaal et al. 2023). The disc around L_2 Pup again lies between these two ranges: warmer than PPDs, colder than post-AGB discs. This is expected as the gas ejected by the AGB star is warm and its high luminosity can provide a lot of dust heating. In post-AGB stars, the stripped star is much warmer, leading to larger temperatures.

4.1.2 Comparison to Homan et al. (2017)

We used a parametric model commonly used for PPDs to model the same observations used by Homan et al. (2017) as we were unable to reproduce their model from the information provided in that work. We did use the same velocity profile of Kervella et al. (2016) and also adopted certain observational parameters of Homan et al. (2017), as described in Section 2.3.

We find three main differences between our model and theirs:

(i) Homan et al. (2017) assumed a three-staged radial temperature profile, which includes an exponential and arctan. This profile includes a feature the authors attribute to the heating of the gas

by the dust disc. The parameter space explored to achieve this fit is not explained. We find that a power-law expression (equation 6) is sufficient to reproduce the observations, indicating that their analytical expression could be overfitted and may have been more complex than needed.

(ii) Homan et al. (2017) retrieved a steep radial density profile at the midplane of $\rho(r, z = 0) \sim r^{-3.1}$, which is much steeper than our $\rho(r, z = 0) \sim r^{-0.4}$ [equations (1), (3), (4)]. The steepness of their density profile does not agree with observations of either PPDs or post-AGB discs. The large difference in density profile could be due to the differences in temperature structures.

(iii) The ^{13}CO abundance retrieved by Homan et al. (2017) is 1×10^{-5}, we find a value of 2×10^{-5} w.r.t. H2. We used the same ^{12}CO abundance of 1×10^{-4} w.r.t. H2. This leads to different ^{12}CO/^{13}CO ratios: 10 by Homan et al. (2017), 5 in this work. While both values lie within the range found by Ramstedt et al. (2014), our value of 5 is on the low side. Optical depth effects might cause such a low ^{12}CO/^{13}CO ratio. Note that photodissociation effects due to differences in self-shielding between the isotopologues would increase the ratio (Saberi, Vlemmings & De Beck 2019). Additionally, a factor of 2 difference is reasonable within the uncertainties of modelling (Ramstedt et al. 2008).

4.1.3 Refining the physical structure: further observations

Besides CO and ^{13}CO, the available ALMA data includes rotational transitions of H2O, ^{29}SiO, ^{30}SiO, SiS, SO, and SO2. The isotopologues of SiO were used to constrain the velocity structure of the disc by Kervella et al. (2016). While the other lines shed some light on the chemical structure of the disc (Sections 4.2 and 4.3), further observations are necessary to better constrain the disc's physical structure, given the differences with Homan et al. (2017) (Section 4.1.2). A better constraint of the physical structure of L₂ Pup's disc will address the differences with the Homan et al. (2017) model and is a crucial input to the chemical model and its predictions.

Spatially resolved emission of abundant optically thin CO isotopologues, such as C^{18}O, C^{17}O, and ^{13}CO (Danilovich et al. 2017; De Nutte et al. 2017), can help determine the disc gas mass and its density distribution more accurately as they probe different layers within the disc. Similarly, H2CO (e.g. Qi, Öberg & Wilner 2013; Pegues et al. 2020), HCN (e.g. Long et al. 2021), HC3N, CH3CN, and C3H2 (e.g. Bergner et al. 2018; Ilee et al. 2021), are well-known temperature probes in PPDs. Our chemical model predicts column densities of 3.72×10^{14}, 8.54×10^{17}, 4.21×10^{13}, 2.80×10^{15}, and 3.65×10^{12} cm^{-2}, respectively, for these molecules.

CH3CN and C3H2 have yet not been detected towards O-rich AGB stars: their detection would put strong constraints on our chemical model. HC3N has only been detected around OH 231.8+4.2, which

has a bipolar outflow with velocities up to ~ 400 km s^{-1} (Velilla Prieto et al. 2015). So far, H2CO has only been detected around the moderate mass-loss rate O-rich AGB star IK Tau with a column density of 2.8×10^{14} cm^{-2}, which is close to our predicted column density (Velilla Prieto et al. 2017). IK Tau likely has a stellar companion shaping its outflow (Coenegrachts et al. 2023). H2CO has also been detected in the Rotten Egg Nebula, an AGB star with an A-type companion (Lindqvist et al. 1992), and the Helix Nebula, which might host an unseen dwarf M star (Gruendl et al. 2001; Tenenbaum et al. 2009; Zack & Ziurys 2013). It seems that detections of H2CO around evolved stars appear to suggest deviations from spherical symmetry.

4.2 Comparison of the chemical model to observations

We qualitatively compare our chemical modelling results with the observations of Kervella et al. (2016). The observed ^{12}CO emission (Appendix A in Kervella et al. 2016) has a radial extent of ~ 9 au and a vertical extent of ~ 3 au. The peak CO abundance predicted by our chemical model lies within ~ 11 au radially and about 2.5 au vertically (Fig. 3). Keeping in mind that we are comparing abundances with observations, the CO abundance predicted by the chemical model is consistent with the observed ^{12}CO emission. A standard set of parent species and their abundances was used as input when running the chemical model. The initial CO abundance in the chemical model is a factor 3 larger than that assumed in the physical model, following Homan et al. (2017) (3×10^{-4} versus 1×10^{-4} w.r.t. H2, Section 3). As we did not a priori know how the chemical abundances would change over time, nor which abundance (profile) to assume when retrieving the physical structure from the observations, we kept these values when calculating the physical and chemical structures. We find that the results of the chemical model are consistent with its independently derived physical structure. The disc averaged CO abundance at 10^5 yr decreased to 2.86×10^{-4} w.r.t. H2.

Besides the ^{12}CO and ^{13}CO $J = 3 - 2$ lines, Kervella et al. (2016) also presented the SO2 ($v = 0$, $J_{K_a, K_c} = 34_{3,31} - 34_{2,32}$), SO ($v = 0$, $N_J = 8_8 - 7_7$), and SiS ($v = 1$, $J = 19 - 18$) lines (their Appendices C–E). The SO2 and SO emission is more extended vertically (about 6 au and ~ 3 au, respectively) compared to the vertically compact SiS emission (up to 2 au). The SO abundance of the chemical model is shown in Fig. 3, that of SO2 and SiS in Fig. C2. At 10^5 yr, the region of highest SO2 abundance has a vertical extent of ~ 6.5 au, that of SO about ~ 5.5 au and of SiS about ~ 1.5 au. The chemical model hence also qualitatively reproduces the relative vertical extents of SO, SO2, and SiS, though a full radiative transfer model is required to check.
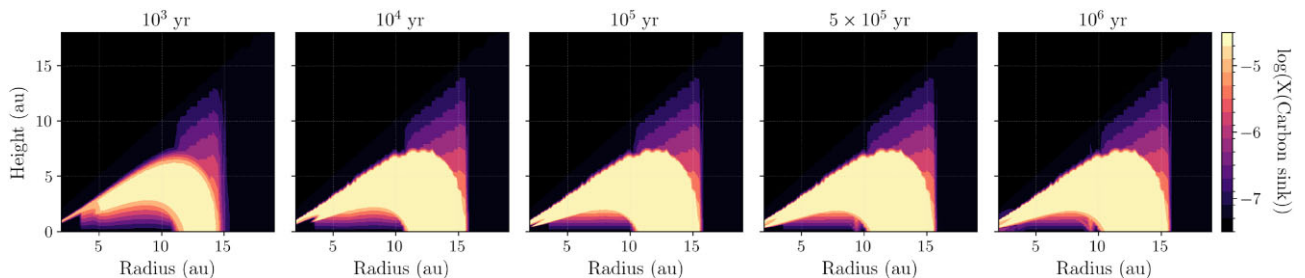
Figure 8. Total fractional abundance of all species with six or more C atoms (called carbon sinks, Section 3.4) in the disc as predicted by the chemical model. The colour map shows the logarithm of the abundance w.r.t. H2. The different columns show the abundance maps after different times, increasing from left to right.

Methanol has been detected towards the post-AGB star HD 101 584 (Olofsson et al. 2017) and OH 2318+4.2, a bipolar nebula around an AGB star (Sánchez Contreras et al. 2018). It is detected in the high-velocity outflows of these objects and is thought to originate from post-shock chemistry, where shocks in the outflow desorb the molecule from an icy grain mantle. The retrieved column densities of CH3OH are $\sim 10^{16}$ and $1 - 8 \times 10^{14}$ cm^{-2}, corresponding to fractional abundances of $\sim 3 \times 10^{-6}$ and $10^{-8} - 10^{-7}$ w.r.t. H2, respectively. Our chemical model predicts a column density of $\sim 10^{14}$ cm^{-2} around 10^5 yr, with a peak fractional abundance around 3×10^{-9} w.r.t. H2. The strongest CH3OH line detected in HD 101584, the 8_{-1} - 7_0 line at 229.759 GHz, is covered by the 2016.1.00207.S. data set (PI P. Kervella), with a peak flux around 80 mJy. It is not clearly detected in the archival L$_2$ Pup data, with an upper limit for the peak flux of around $2 - 3$ mJy. From running a simplified radiative transfer calculation, using the accelerated lambda iteration method code (ALI, e.g. Danilovich et al. 2021, with molecular data from Rabli & Flower 2010), based on the spherically symmetric model of Danilovich et al. (2015) and assuming a Gaussian abundance profile with an *e*-folding radius of 10^{15} cm, we determine that for a methanol abundance of 3×10^{-9} w.r.t. H2 (the maximum abundance predicted by the chemical model) the 8_{-1} - 7_0 line would not be detected above the noise for L$_2$ Pup. The non-detection of CH3OH in L$_2$ Pup could be due to its lower abundance or due to a different excitation mechanism, as methanol is formed in the warm inner midplane of the disc via gas-phase reactions rather than via shock chemistry in a high-velocity outflow, as in the two other objects. Further observations are necessary to confirm the (non)detection of methanol in L$_2$ Pup's disc.

A radiative transfer analysis of the chemical model predictions lies outside the scope of this paper. Moreover, it is important to note that the predicted chemistry depends on the input physical structure. A parameter study to quantify the impact of different physical structures on the chemistry is computationally intensive and will be addressed in future work. As stated in Section 4.1.3, further observations are necessary to constrain the retrieved physical model of L$_2$ Pup's disc.

4.3 Age of the disc

After 5×10^5 yr, the chemical model predicts a gap in the inner midplane for SO and SO2 (Figs 3 and C2), which is about 1 au in height and 9 au radially for both molecules. Such a gap is not seen in the emission maps of SO2 ($v = 0$, $J_{K_a, K_c} = 34_{3,31} - 34_{2,32}$) and SO ($v = 0$, $N_J = 8_8 - 7_7$, Appendices C and D in Kervella et al. 2016). The beam size of the observations is 17.7×14.5 mas $\approx 1.1 \times 0.9$ au. The gap predicted by the chemical models should hence be observable, especially as the upper energy level of the SO2 transition is 582 K. Therefore, under the assumptions of our chemical model of a disc that is formed at a specific time and then evolves in isolation of the outflow, we expect it to be not older than 10^5 yr. Hydrodynamical simulations suggest that while the disc is formed on a time-scale of a few 100 yr, some outflowing gas will still be captured by and incorporated into the disc (Chen et al. 2016). If the disc is continually refreshed with new material, its age could be older.

L$_2$ Pup is currently in the thermally pulsing-AGB (TP-AGB) phase (Kervella et al. 2016), which is a short-lived phase of about 0.5×10^5 yr (Rosenfield et al. 2014). Assuming a static model, the disc could therefore both be a remnant from the early-AGB phase or have originated in the TP-AGB phase. The timeframe of 10^5 yr is too short

for the massive planet to have been formed within this disc (which would take ~ 10 Myr if formed via core accretion; Pollack et al. 1996), and is likely to be a first-generation planet present before the AGB phase.

4.4 Chemistry within the AGB disc

The chemistry within the disc around L$_2$ Pup is different to that in a low-density O-rich outflow both in distribution and composition. The only similarity is the lack of dust–gas chemistry, although this is due to different factors. In the outflow, the density is too low for gas-phase species to efficiently accrete onto the dust. The density in the disc midplane is at least four orders of magnitude larger, but the dust temperature is too high for accreted ices to remain on the dust surface. The dust temperature was taken to be that of the gas, a reasonable assumption given the density of the disc. However, a lower dust temperature could result in the depletion of gas-phase species and the formation of ices.

To compare the chemical composition of the disc to that of the outflow, we use the ratio of their column densities. This column density ratio is weighted by their respective CO column densities,

$$\text{Ratio} = \frac{\bar{N}_X}{\bar{N}_{\text{CO}}} \times \frac{N_{\text{CO}}}{N_X}, \tag{9}$$

with $\bar{N}_X$ the disc-averaged column density of species X (equation 8) and N_X the column density of species X in the outflow. This normalizes the ratio to the most abundant molecule (after H2), allowing for a better comparison between the chemistries of these different density distributions. The CO column density ratio, $\bar{N}_{\text{CO}}/N_{\text{CO}}$, is ~ 100 for all times in the disc model, decreasing from 126 at 10^3 yr to 98 at 10^6 yr.

The chemical composition of the disc is different from that of the outflow: the disc does not simply inherit the initial composition, but also significantly modifies the abundances of parent and daughter species. Unlike in the outflow and despite its O-rich composition, numerous C-bearing molecules are abundantly formed throughout the disc, including COMs. Two main chemical regions can be distinguished: (i) the dense midplane, where chemistry is initiated by cosmic rays, and (ii) the outer edge, where it is initiated by interstellar UV photons. Within the outer region, the hot inner edge displays a different chemistry than the cooler outer regions. The chemistry in the dense midplane differs from that in a PPD because of the higher temperatures in the disc, while the chemistry of the outer regions is different to an AGB outflow due to the higher densities in this region.

Fig. 9 shows the column density ratio for a set of species which have a column density larger than 10^{10} cm^{-2} at some time in the disc and which show a difference of at least an order of magnitude at some time in the disc chemical model. Their abundance profiles are shown in Fig. C4 and the absolute values of their column densities are shown in Fig. C5. These species can be regarded as chemical tracers of the presence of a disc structure. The left panel shows species which have a smaller column density in the disc model compared to the outflow model, the right panel shows those which have a larger column density. The shaded regions group species originating from different types of chemistry: midplane (cosmic ray) chemistry is highlighted in blue, outer edge (photo) chemistry in orange, with species present in the hot inner edge highlighted in dark orange. Species formed via both cosmic ray and photochemistry are placed in the blue region with a boldface label. Sections 4.4.1 and 4.4.4 elaborate on the cosmic-ray induced chemistry in the midplane and in the photochemistry in outer regions, respectively.
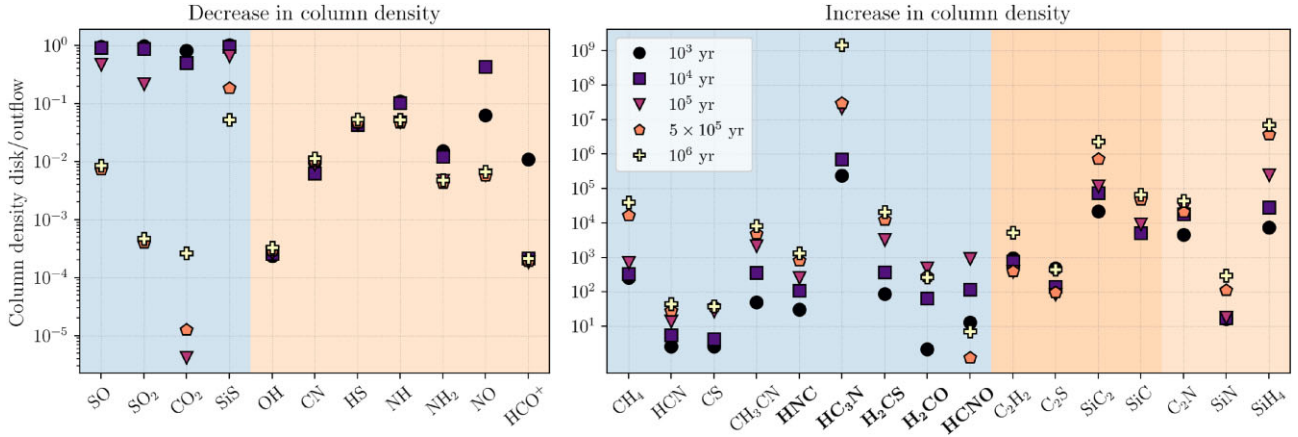
Figure 9. Ratio of the disc column density relative to CO over the outflow column density relative to CO (equation 9) for species that show a decrease (left panel) and increase in column density relative to the outflow (right panel) of more than an order of magnitude at any time in the disc chemical model. Different markers and colours show the ratio at different times for the disc model. The shaded regions group species originating from different types of chemistry. Blue: midplane (cosmic ray) chemistry, orange: outer edge (photo) chemistry, dark orange: hot inner edge. Boldfaced labels denote species that are formed via cosmic ray and photochemistry. These species can be regarded as chemical tracers of the disc.

4.4.1 Cosmic-ray induced chemistry

Cosmic rays dissociate parent species in the midplane, liberating atoms which participate in a rich chemistry thanks to the high densities in this region. A large role is played by the reactive C, produced mostly by the destruction of the parent CO. Species whose column density is significantly impacted by this chemistry are shown in the blue shaded regions of Fig. 9.

4.4.2 Decrease in column density relative to the outflow

Reactions between C and the parents SO and SO_2 form CS, leading to a gap in abundance in the dense midplane and a lower column density relative to the outflow. At 10^5 yr, their column densities are ~ 5 and ~ 9 times smaller than in the outflow, increasing to 100 times and $\sim 7 \times 10^3$, respectively. CO_2 shows a similar gap in the midplane, which is caused by reactions with Si forming SiO. Its column density is more than five orders of magnitude smaller than in the outflow at 10^5 yr. At longer time-scales, this difference is reduced to roughly three orders of magnitude thanks to its reformation by collisional dissociation of HCOOH (see below).

The decrease in column density of SiS, reaching about an order of magnitude after 5×10^5 yr, is caused by reactions with H_3+, a product of cosmic-ray interactions. The resulting $HSiS+$ reacts with the parent H_2O, producing $SiOH+$ which goes on to react with the parent NH_3, funnelling Si away from SiS into SiO.

4.4.3 Increase in column density relative to the outflow

Hydrogen is efficiently added to carbon at the high densities and temperatures in the midplane, forming CH_4. Its column density is about three orders of magnitude larger in the disc. CH_4 reacts with $N+$, formed via cosmic rays, producing $HCNH+$. This molecule then reacts with H_2S and NH_3 to form HCN and HNC, with column densities more than 1 and 3 orders of magnitude larger than in the outflow, respectively. The CS abundance increases thanks to the reactions of C with SO_2 and SO, increasing its column density by about 1 order of magnitude.

$HCO+$ is produced by cosmic ray chemistry via $H_3+ + CO$. Radiative association of $HCO+$ with H_2O yields $HCOOH_2+$, which

reacts with H_2O and NH_3 to form HCOOH (increase in column density $\gtrsim 4$ orders of magnitude compared to the outflow).

The CH_3+ cation plays a crucial role in the chemistry of the midplane. It is formed via $CH_4 + He+$, both products of cosmic rays, forming CH_2+ which reacts with H_2 to CH_3+. The formation of all detected COMs (and HC_3N) is linked to this cation. The high densities of the midplane allow for the slow radiative association reactions, dissociative recombination with dust, and collisional dissociation reactions in these pathways to be efficient. The main formation pathways of COMs via reactions with CH_3+ are:

(i) Radiative association between the parent HCN and CH_3+ yields CH_3CNH+, which dissociatively recombines with negatively charged dust grains to form CH_3CN (increase in column density of $\gtrsim 3$ orders of magnitude at 10^5 yr compared to the outflow).

(ii) NH_3 can radiatively associate with CH_3+ forming CH_3NH_3+, which dissociatively recombines with dust to CH_3NH_2 (column density $\gtrsim 6$ orders of magnitude). The association with CH_3+ also forms C_2H_5CNH+, which dissociatively recombines with dust to C_2H_5CN ($\gtrsim 6$ orders of magnitude). A sequence of collisional dissociations and reactions with C lead to the formation of CH_2CCH, which reacts with N to form HC_3N ($\gtrsim 7$ orders of magnitude).

(iii) Reactions of CH_3+ with the parent H_2O gives CH_3OH_2+, which produces CH_3OH by reacting with the parent NH_3 ($\gtrsim 3$ orders of magnitude). Subsequent reaction with H_2CO results in $H_5C_2O_2+$, which dissociatively recombines with dust to $HCOOCH_3$ ($\gtrsim 8$ orders of magnitude).

(iv) The formation of methanol initiates the production of H_2CO, increasing its column density by almost 3 orders of magnitude at 10^5 yr, which is formed by collisional dissociation of CH_2OH and CH_3O. Both have their origin in the $CH_3 + +H_2O$ reaction, which forms both CH_3OH and CH_3OH_2+. CH_2OH is formed via $CH_3OH + H$, CH_3O is formed after CH_3OH_2+ reacting with CH_3OH followed by dissociative recombination with dust and collisional dissociation.

Other species formed by the successive addition of hydrogen to carbon also play an active role in the cosmic-ray induced midplane chemistry. The column density of H_2CS increases by more than 3 orders of magnitude at 10^5 yr. It is formed via $CH_4 + S+$ (both with a cosmic-ray origin) producing H_3CS+, which then dissocia-

tively recombines with dust. HNCO is formed by CH2 + NO and C2H5CN + OH, with a increased column density of about 3 orders of magnitude at 10^5 yr. The formation of HC3N is kickstarted by CH4 + CH3+, forming C2H5+, which yields C2H4 after reaction with the parents H2O and H2S. Subsequent reactions with C and N finally produce HC3N.

4.4.4 Interstellar UV photochemistry

The chemistry in the more tenuous outer regions of the disc is a rich photochemistry initiated by interstellar UV photons. However, because of the higher densities and temperatures of the disc, the products of this photochemistry are different to those of the photochemistry taking place in the outer regions of the outflow. C2H2 plays an important role in the chemistry of the outer regions of the disc. It is formed by the successive addition of hydrogen to C (produced by photodissociation of mainly the parent CO) into CH, which then reacts with C again to form C2. These reactions lead to the formation of C2H and finally C2H2. Species whose column density is significantly impacted by this chemistry are shown in the orange shaded regions of Fig. 9.

4.4.5 Decrease in column density relative to the outflow

The daughters OH, CN, HS, NH, and NH2 are all first-generation daughters formed by photodissociation of the parents H2O, HCN, H2S, and NH3. They are present in a shell in the outer disc. Their main destruction mechanisms are photodissociation and reaction with H2 to reform the parent species in a photodissociation – hydrogen addition loop, depending on the density. The significant decreases in their column densities relative to the outflow is caused by reactions funnelling them away from their parents.

Reactions with C-bearing species remove OH and CN from their photodissociation – hydrogen addition loops, reducing their column densities by $\sim 5 \times 10^3$ and 2 orders of magnitude, respectively. OH mainly reacts with C to reform CO and with CH2 to produce H2CO, which is also formed by O + CH3. CN is involved in reactions with C2H2 and C2H4, producing cyanopolyynes and CN-bearing C-chains.

The column densities of HS, NH, and NH2 decrease between one and two orders of magnitude relative to the outflow. S is removed from the photodissociation–hydrogen addition loop by the formation of CS via HS + C and S+CH2, and by the formation of H2CS via S+CH3. NH reacts with O to produce NO, which is then efficiently destroyed by Si forming SiO and NH forming N2O, which photodissociates into N2. Subsequently, the column density of NO is about two orders lower in the disc after 10^5 yr. NH also efficiently reacts with S to produce NS, which then reacts with O to form NO and SO.

The column density of the cation HCO+ is almost 4 orders of magnitude smaller in the disc. Its main formation mechanism is C + +H2O. However, unlike in the outflow, C+ is also involved in the C-chain chemistry in this region, which reduces the HCO+ abundance.

4.4.6 Increase in column density relative to the outflow

The column density of C2H2 increases by about 3 orders of magnitude due to photochemistry in the outer regions of the disc. As stated earlier, C2H2 plays an important role in the chemistry in this region. Reactions with SO+, formed by photoionization of SO and by OH + S+, produce C2S, the column density of which increases

by two to three orders of magnitude. Reactions with Si, liberated by photodissociation of the parent SiO, produce SiC2, whose column density increases by some 5 orders of magnitude at 10^5 yr. SiC is a product of SiC2 + O, with the latter produced mostly via the photodissociation of the parents H2O and SiO.

These four species (C2H2, C2S, SiC2, and SiC) show large abundances at the inner edge of the disc, within the first few au (marked by the dark orange region in Fig. 9). This is caused by the strong temperature dependence of the H2 + C2H reaction: its reaction rate depends on temperature as $T^{2.57}$ (Laufer & Fahr 2004). This has a significant effect at the large temperatures in this region (between 1100 and 1750 K). Even though the Si + C2H2 reaction has a negative temperature dependence ($T^{-0.71}$; Canosa et al. 2001), the large increase in C2H2 abundance leads to a larger SiC2 and SiC abundance in this region.

The formation of SiN and SiH4 is linked to Si. The SiN column density is about an order of magnitude larger than in the outflow at 10^5 yr. Its production is started by NH3 + Si+, with the latter produced by the photoionization of Si or charge exchange with S+. This reaction forms SiNH2+ which dissociatively recombines with electrons to SiN or recombines to HNSi, which is then photodissociated into SiN. Closer to the midplane, the cation dissociatively recombines with negatively charged dust grains. The SiH4 column density is more than 5 orders of magnitude larger at 10^5 yr. It is formed by the successive addition of hydrogen to SiH+ into SiH5+, which then reacts with H2O or dissociatively recombines with electrons to SiH4. SiH+ is formed by Si + H3O+, with the latter formed by the addition of H to H2O+, a product of the photoionization of H2O.

5 CONCLUSIONS

We presented an updated model of the density and temperature of the disc around L$_2$ Pup by fitting archival ALMA ^{12}CO and ^{13}CO $J = 3 - 2$ lines. The disc has a surface density profile $\Sigma(r) \sim r^{-1}$ and is warm, with a midplane temperature of 900 K and $T_{\rm mid}(r) \sim r^{-0.2}$. Unlike Homan et al. (2017), we do not require a three-staged radial temperature profile or an extremely steep vertical density profile (our $\rho(r) \sim r^{-0.4}$ versus their $\sim r^{-3.1}$). A more simple parametrization used commonly for PPDs is able to reproduce the observations.

The chemical model presented in this paper is the first chemical model of a disc around an AGB star, specifically of L$_2$ Pup's disc. The physical structure of the disc has a large impact on its chemistry. All species are constrained to the disc, within $\sim$ 15 au radially and $\sim$ 10 au vertically. This is much smaller than the extent of the parents' envelope in the outflow, which ranges from 30–3000 au radially from the star and is also where the peak abundances of the daughter species are located.

The chemistry within the disc leads to large abundances of C-bearing molecules, a surprising result given its O-rich composition. Certain COMs are abundantly formed in the midplane. Unlike in PPDs, these are formed purely via gas-phase chemistry as dust-gas chemistry does not play a role at the high temperatures of L$_2$ Pup's disc. C-chains are readily formed in the outer regions, though caution is needed as the chemical network does not include fully saturated long (more than three C atoms) carbon-chain species. Two chemical regimes can be distinguished: cosmic-ray induced chemistry in the midplane and photoinduced chemistry in the outer regions. The abundances of species are significantly increased or decreased with respect to an O-rich outflow chemical model, allowing us to identify potential and unique tracers of the disc such as H2CO, CH3CN, and HC3N. Moreover, the chemical model can be used to constrain the age of the disc. The appearance of a gap in abundance in the

midplane of SO and SO2 after 5×10^5 yr appears to suggest that the disc around L$_2$ Pup is about 10^5 yr old, as these features were not observed in the data presented by Kervella et al. (2016).

Further observations are necessary to further constrain the physical structure of the disc. In particular, optically thin CO isotopologues are needed to better pin down the disc mass and density structure, while species such as H2CO, HC3N, CH3CN, and C3H2 can be used as empirical temperature probes. Targeting the tracers of the midplane and outer region chemistries will provide an essential test of the chemical model predictions.

Our unique chemical model clearly shows the impact that large-scale structures within an AGB outflow can have on its chemistry. This exploratory work paves the way for a more general study of AGB discs, ranging in density and temperature structures. However, note that the 2D model used in this work predicts the chemistry assuming a fixed density structure; coupling chemistry to a hydrodynamical model is necessary to take the effect of dynamical evolution of the chemistry into account.

ACKNOWLEDGEMENTS

DATA AVAILABILITY

The data underlying this article will be shared on reasonable request to the corresponding author.

REFERENCES

Agúndez M. et al., 2017, A&A, 601, A4
Agúndez M., Martínez J. I., de Andres P. L., Cernicharo J., Martín-Gago J. A., 2020, A&A, 637, A59
Andrews S. M., 2020, ARA&A, 58, 483
Andrews S. M., Wilner D. J., Hughes A. M., Qi C., Dullemond C. P., 2009, ApJ, 700, 1502
Baulch D. L. et al., 2005, J. Phys. Chem. Ref. Data, 34, 757
Bergner J. B., Guzmán V. G., Öberg K. I., Loomis R. A., Pegues J., 2018, ApJ, 857, 69
Bohlin R. C., Savage B. D., Drake J. F., 1978, ApJ, 224, 132

Brown J. M., Millar T. J., 2003, MNRAS, 339, 1041
Canosa A., Le Picard S. D., Gougeon S., Rebrion-Rowe C., Travers D., Rowe B. R., 2001, J. Chem. Phys., 115, 6495
Chen Z., Nordhaus J., Frank A., Blackman E. G., Balick B., 2016, MNRAS, 460, 4182
Coenegrachts A., Danilovich T., De Ceuster F., Decin L., 2023, A&A, 678, A85
Cordiner M. A., Millar T. J., 2009, ApJ, 697, 68
Corporaal A., Kluska J., Van Winckel H., Andrych K., Cuello N., Kamath D., Mérand A., 2023, A&A, 674, A151
Danilovich T. et al., 2015, A&A, 581, A60
Danilovich T., Lombaert R., Decin L., Karakas A., Maercker M., Olofsson H., 2017, A&A, 602, A14
Danilovich T. et al., 2021, A&A, 655, A80
Danilovich T. et al., 2024, Nat. Astron., 8, 308
De Ceuster F., Homan W., Yates J., Decin L., Boyle P., Hetherington J., 2020a, MNRAS, 492, 1812
De Ceuster F. et al., 2020b, MNRAS, 499, 5194
De Ceuster F. et al., 2022, J. Open Source Softw., 7, 3905
De Nutte R. et al., 2017, A&A, 600, A71
Decin L., 2021, ARA&A, 59, 337
Decin L. et al., 2020, Science, 369, 1497
Gruendl R. A., Chu Y.-H., O'Dwyer I. J., Guerrero M. A., 2001, AJ, 122, 308
2003, Habing H. J., Olofsson H., eds, Asymptotic Giant Branch Stars. A&A Library, Springer, New York
Hartmann L., Calvet N., Gullbring E., D'Alessio P., 1998, ApJ, 495, 385
Heays A. N., Bosman A. D., van Dishoeck E. F., 2017, A&A, 602, A105
Hillen M. et al., 2014, A&A, 568, A12
Hillen M., de Vries B. L., Menu J., Van Winckel H., Min M., Mulders G. D., 2015, A&A, 578, A40
Höfner S., Olofsson H., 2018, A&A, 26, 1
Homan W., Richards A., Decin L., Kervella P., de Koter A., McDonald I., Ohnaka K., 2017, A&A, 601, A5
Ilee J. D. et al., 2021, ApJS, 257, 9
Ireland M. J., Tuthill P. G., Bedding T. R., Robertson J. G., Jacob A. P., 2004, MNRAS, 350, 365
Karakas A. I., Lugaro M., 2016, ApJ, 825, 26
Kervella P. et al., 2014, A&A, 564, A88
Kervella P. et al., 2015, A&A, 578, A77
Kervella P., Homan W., Richards A. M. S., Decin L., McDonald I., Montargès M., Ohnaka K., 2016, A&A, 596, A92
Khouri T. et al., 2016, A&A, 591, A70
Kluska J., Hillen M., Van Winckel H., Manick R., Min M., Regibo S., Royer P., 2018, A&A, 616, A153
Laufer A. H., Fahr A., 2004, Chem. Rev., 104, 2813
Leão I. C., de Laverny P., Mékarnia D., de Medeiros J. R., Vandame B., 2006, A&A, 455, 187
Lindqvist M., Olofsson H., Winnberg A., Nyman L. A., 1992, A&A, 263, 183
Long F. et al., 2021, A&A, 647, A118
Lykou F. et al., 2015, A&A, 576, A46
Lynden-Bell D., Pringle J. E., 1974, MNRAS, 168, 603
Maercker M. et al., 2012, Nature, 490, 232
Mauron N., Huggins P. J., 2006, A&A, 452, 257
McElroy D., Walsh C., Markwick A. J., Cordiner M. A., Smith K., Millar T. J., 2013, A&A, 550, A36
Millar T. J., Walsh C., Van de Sande M., Markwick A. J., 2024, A&A, 682, A109
Ohnaka K., Schertl D., Hofmann K. H., Weigelt G., 2015, A&A, 581, A127
Olofsson H. et al., 2017, A&A, 603, L2
Pegues J. et al., 2020, ApJ, 890, 142
Pollack J. B., Hubickyj O., Bodenheimer P., Lissauer J. J., Podolak M., Greenzweig Y., 1996, Icarus, 124, 62
Qi C., Öberg K. I., Wilner D. J., 2013, ApJ, 765, 34
Rabli D., Flower D. R., 2010, MNRAS, 406, 95

Ramstedt S., Schöier F. L., Olofsson H., Lundgren A. A., 2008, A&A, 487, 645

Ramstedt S. et al., 2014, A&A, 570, L14

Rosenfield P. et al., 2014, ApJ, 790, 22

Saberi M., Vlemmings W. H. T., De Beck E., 2019, A&A, 625, A81

Sánchez Contreras C., Alcolea J., Bujarrabal V., Castro-Carrizo A., Velilla Prieto L., Santander-García M., Quintana-Lacaci G., Cernicharo J., 2018, A&A, 618, A164

Siebert M. A., Van de Sande M., Millar T. J., Remijan A. J., 2022, ApJ, 941, 90

Tenenbaum E. D., Milam S. N., Woolf N. J., Ziurys L. M., 2009, ApJ, 704, L108

Van de Sande M., Millar T. J., 2022, MNRAS, 510, 1204

Van de Sande M., Sundqvist J. O., Millar T. J., Keller D., Homan W., de Koter A., Decin L., De Ceuster F., 2018, A&A, 616, A106

Van de Sande M., Walsh C., Millar T. J., 2021, MNRAS, 501, 491

Van de Sande M., Walsh C., Millar T. J., 2023, Faraday Discuss., 245, 586

van Leeuwen F., 2007, A&A, 474, 653

Velilla Prieto L. et al., 2015, A&A, 575, A84

Velilla Prieto L. et al., 2017, A&A, 597, A25

Velilla-Prieto L. et al., 2023, Nature, 617, 696

Walsh C., Nomura H., van Dishoeck E., 2015, A&A, 582, A88

Williams J. P., Best W. M. J., 2014, ApJ, 788, 59

Williams J. P., Cieza L. A., 2011, ARA&A, 49, 67

Zack L. N., Ziurys L. M., 2013, ApJ, 765, 112

APPENDIX A: ALMA OBSERVATIONS

Moment 0 maps of the ^{12}CO and ^{13}CO $J = 3 - 2$ lines are presented in Kervella et al. (2016) (their figs A1 and B1). Here, we present channel maps of these lines with beam information.
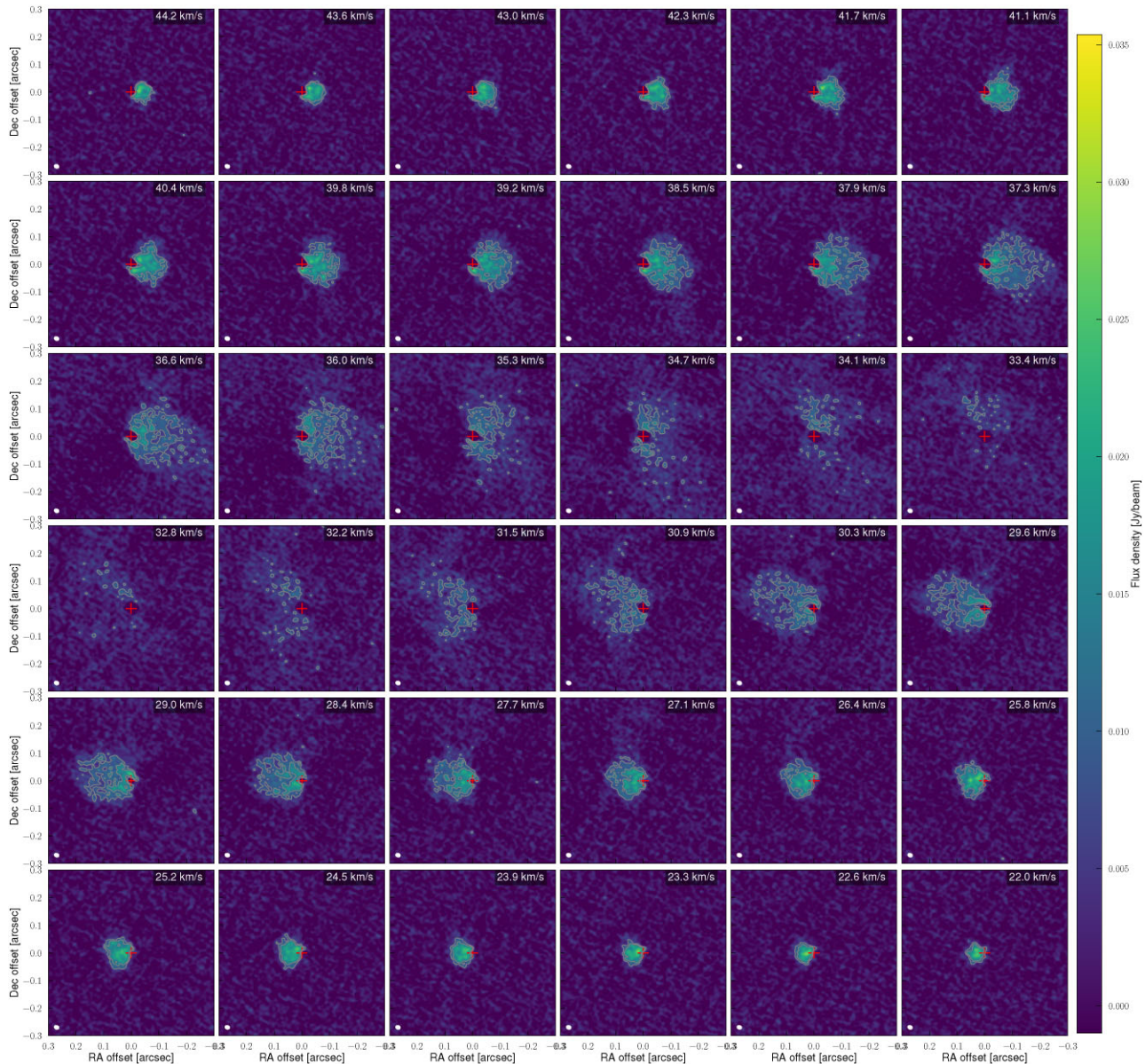
Figure A1. Channel maps of ^{12}CO $J = 3 - 2$ emission toward L$_2$ Pup. The grey contours show flux levels at 3 and 5 times the rms noise. The beam is shown in white in the bottom left hand corners.
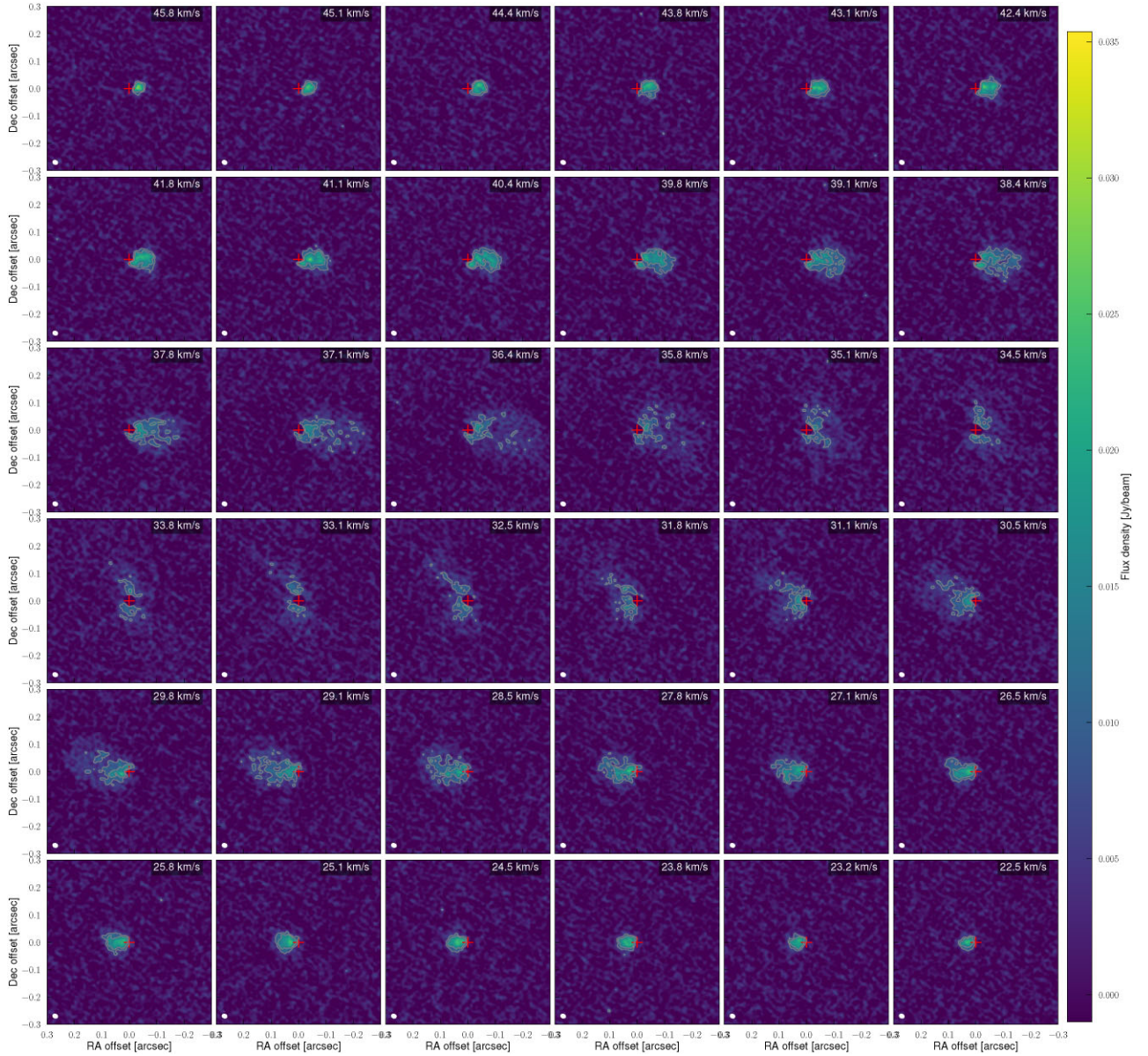
Figure A2. Channel maps of ^{13}CO $J = 3 - 2$ emission towards L$_2$ Pup. The grey contours show flux levels at 3 and 5 times the rms noise. The beam is shown in white in the bottom left hand corners.

APPENDIX B: MAGRITTE MODELLING RESULTS
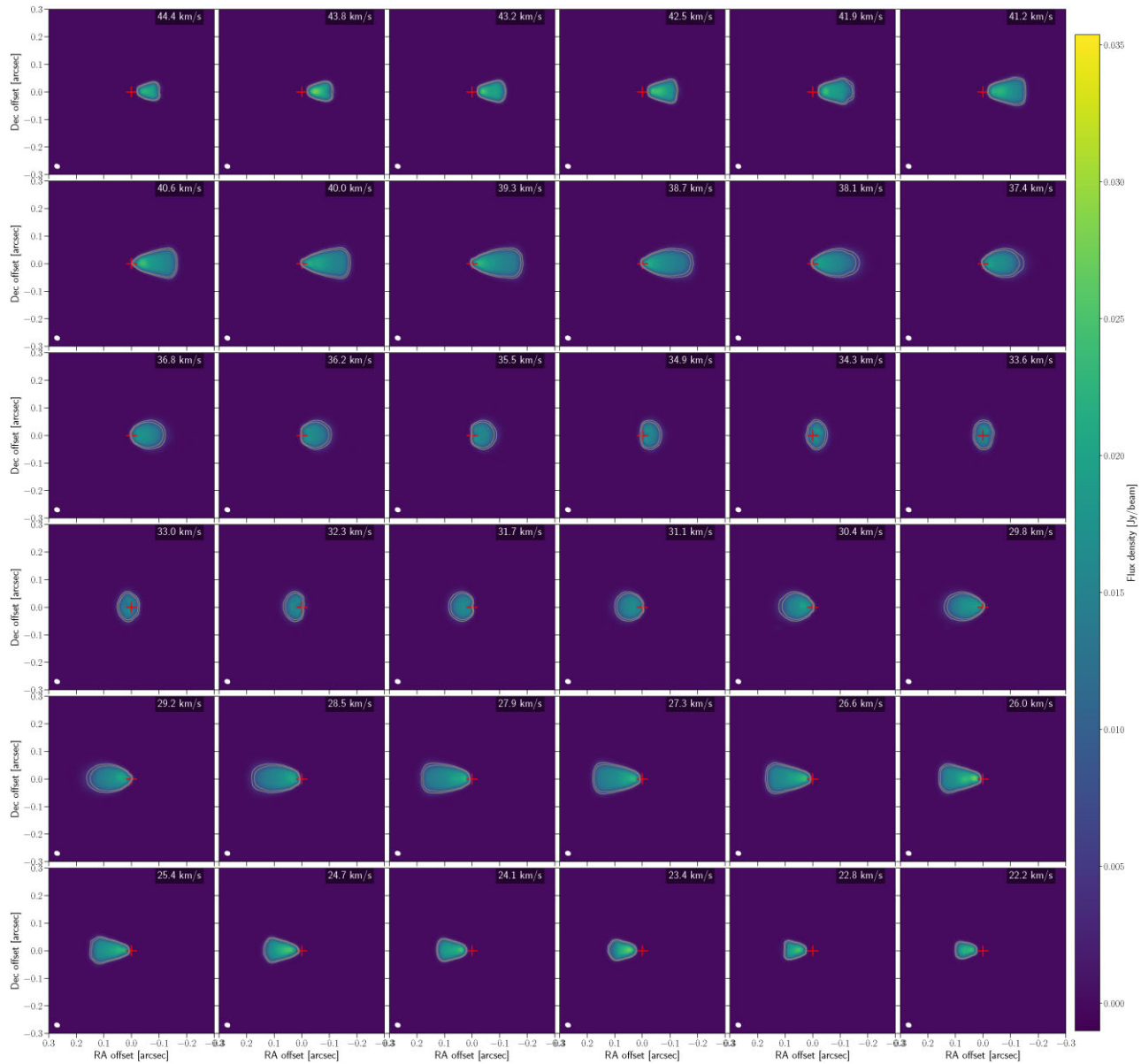
Figure B1. Modelled channel maps of ^{12}CO $J = 3 - 2$ emission toward L_2 Pup. The grey contours show flux levels at 3 and 5 times the rms noise. The beam is shown in white in the bottom left hand corners. Model parameters are listed in Table 1.
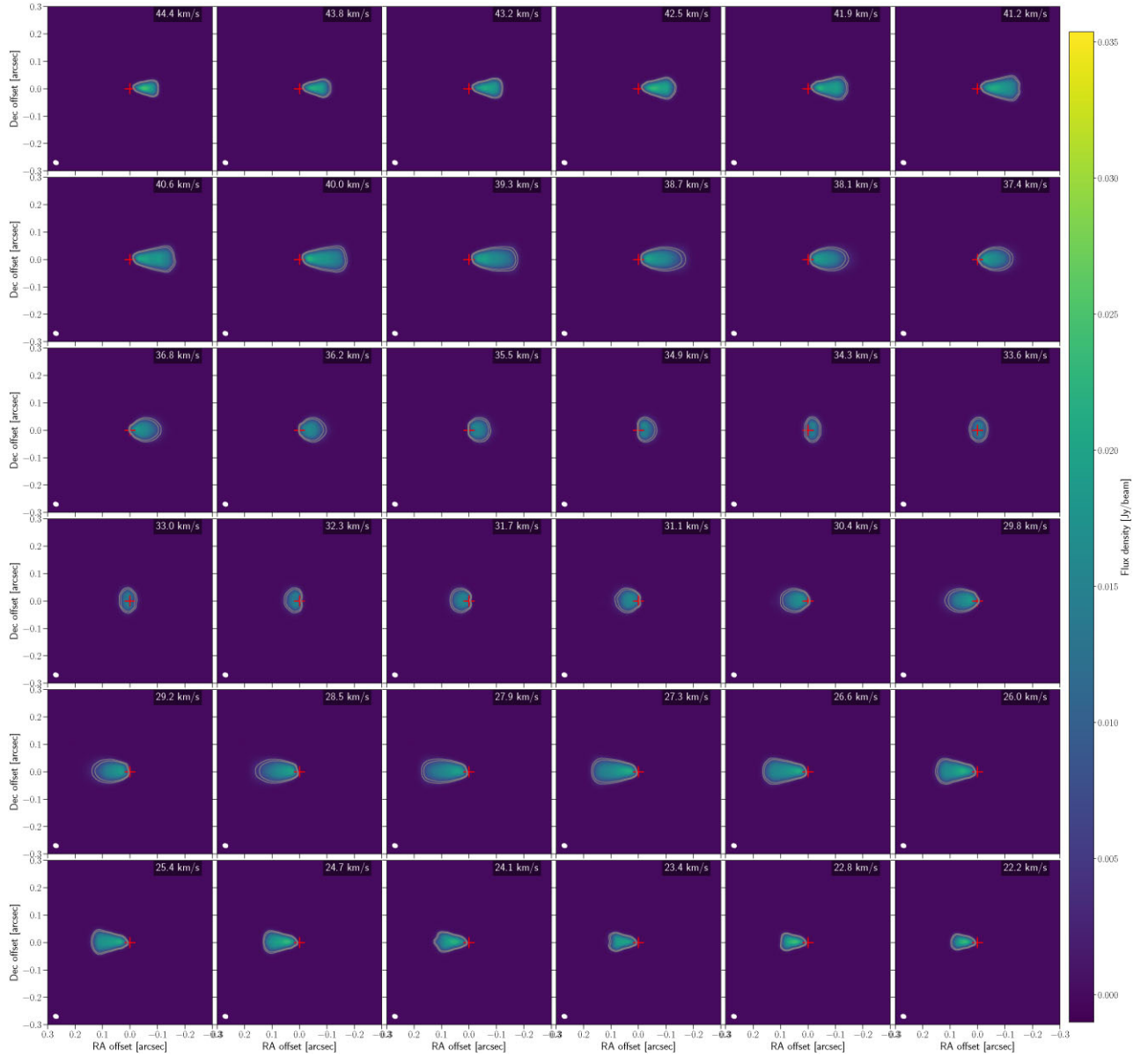
Figure B2. Modelled channel maps of ^{13}CO $J = 3 - 2$ emission toward L$_2$ Pup. The grey contours show flux levels at 3 and 5 times the rms noise. The beam is shown in white in the bottom left hand corners. Model parameters are listed in Table 1.
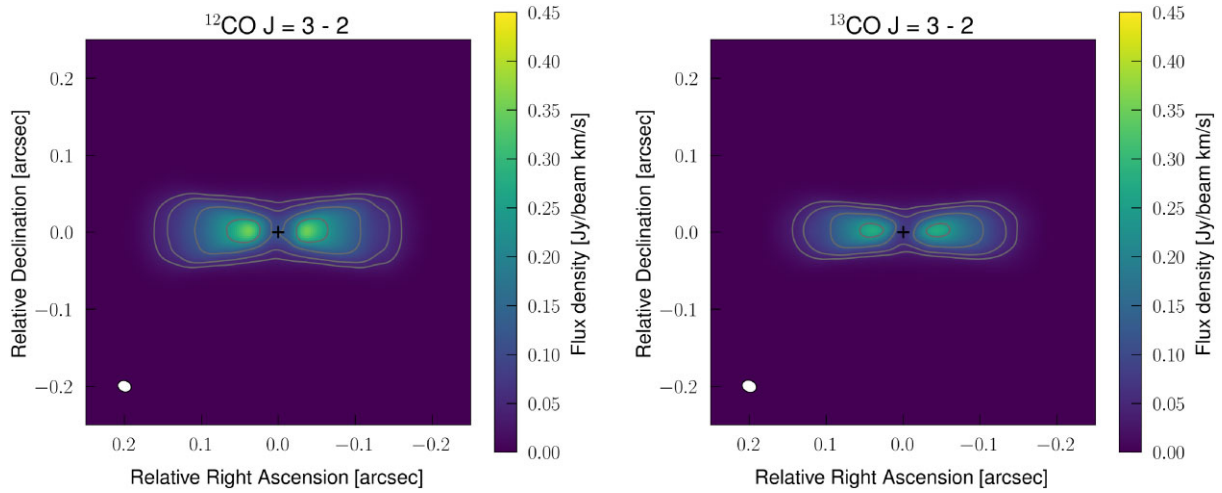
Figure B3. Modelled moment 0 map of ^{12}CO (left) ^{13}CO $J = 3 - 2$ (right). The grey contours show flux levels at 3, 5, 10, 20, and 30 times the rms noise. The beam is shown in white in the bottom left hand corners. Model parameters are listed in Table 1.

APPENDIX C: CHEMICAL MODEL RESULTS
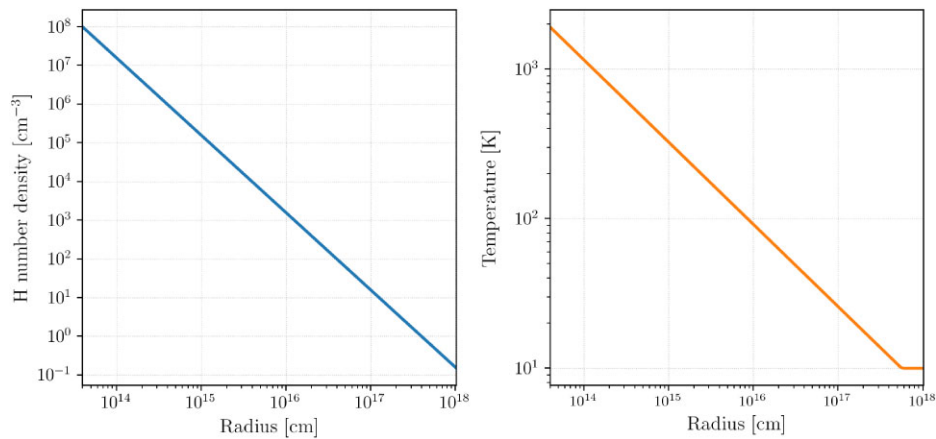
Figure C1. The H2 number density (left) and temperature (right) assumed throughout the outflow chemical model (Section 3).
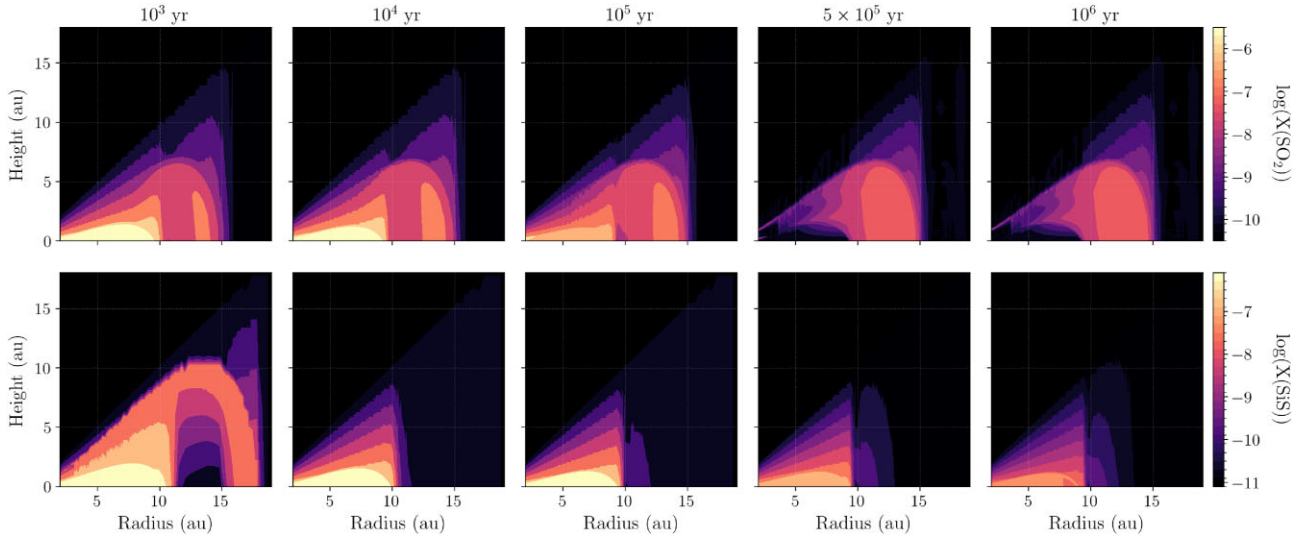
Figure C2. Fractional abundance of SO2 (top row) and SiS (bottom row) throughout the disc as predicted by the chemical model. The colour map shows the logarithm of the abundance w.r.t. H2. The different columns show the results after different times, increasing from left to right.
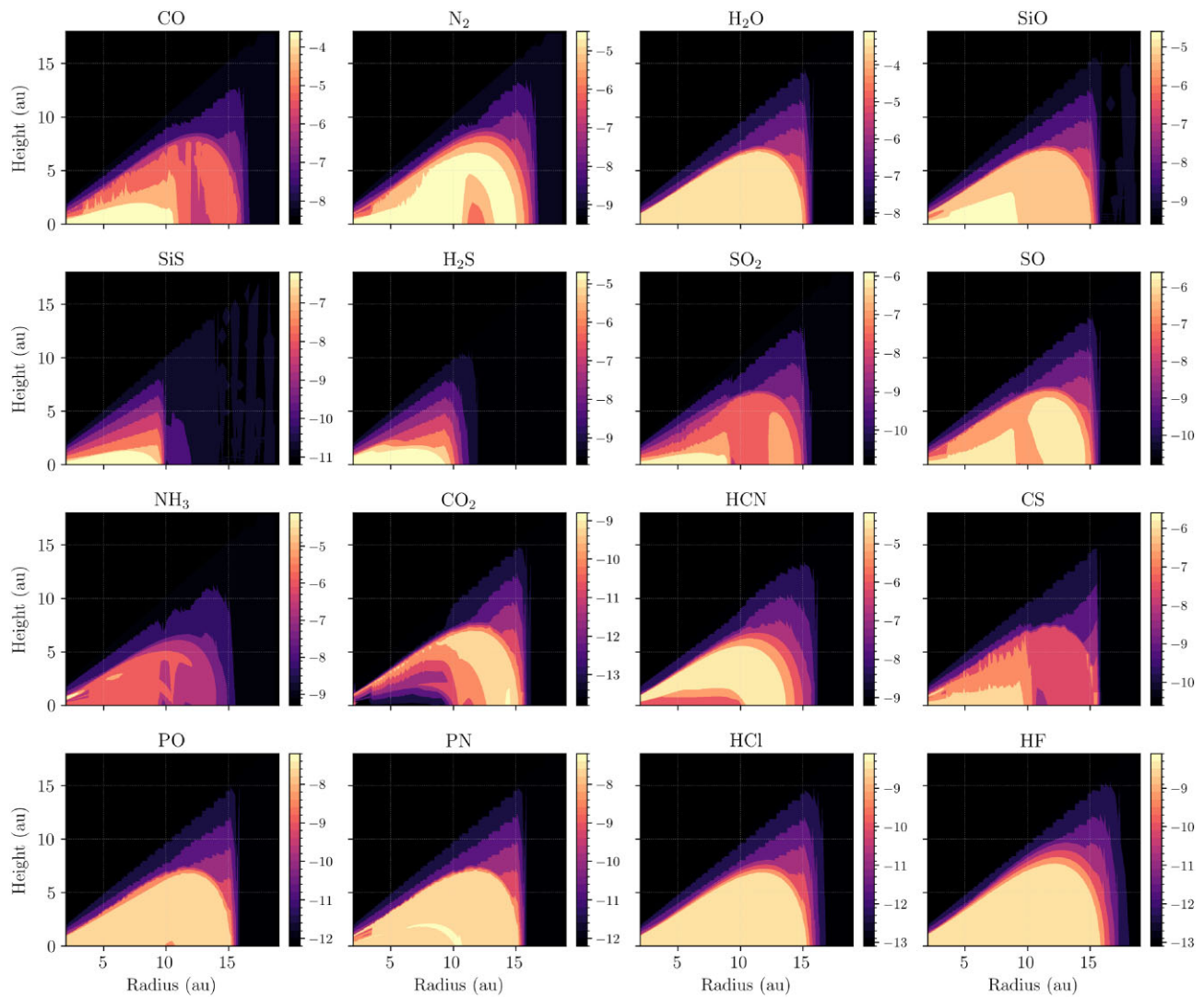
Figure C3. Fractional abundances of the parent species throughout the disc as predicted by the chemical model of the parent species after 10^5 yr. The colour map shows the logarithm of the abundance w.r.t. H2. Note that each colour map has a different dynamic range.
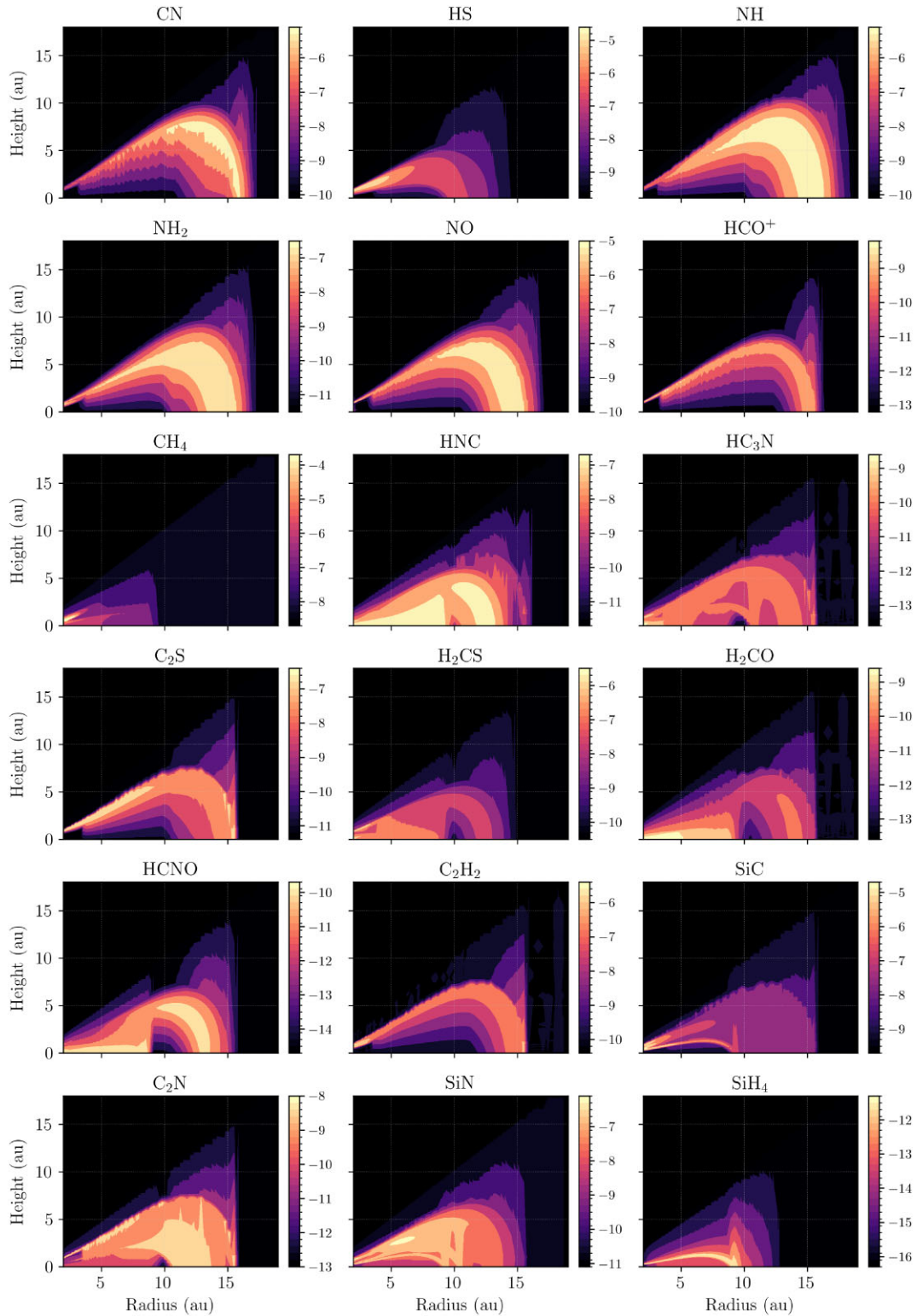
Figure C4. Fractional abundances of some daughter species shown in Fig. 9 throughout the disc as predicted by the chemical model of the parent species after 10^5 yr. The colour map shows the logarithm of the abundance w.r.t. H2. Note that each colour map has a different dynamic range.
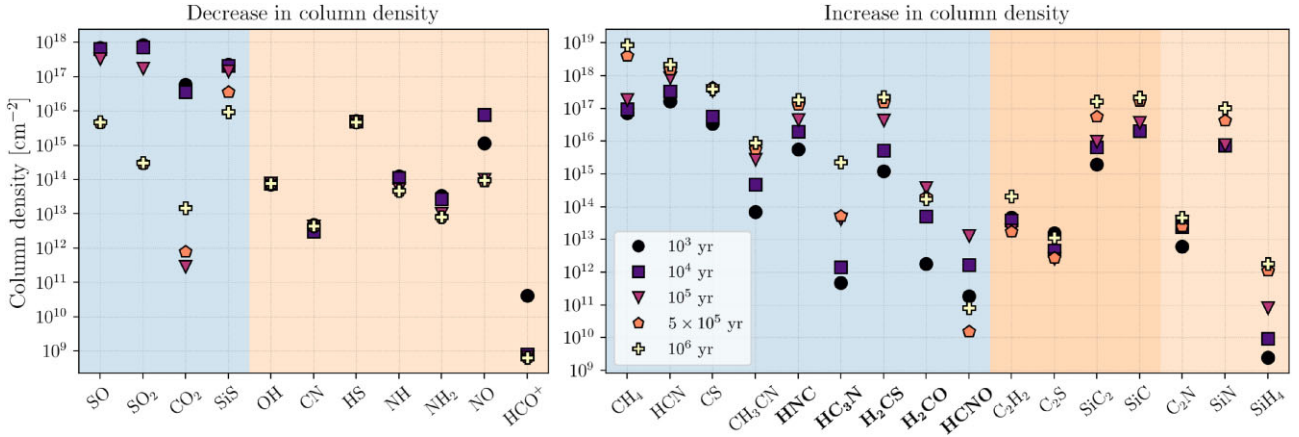
Figure C5. Disc column density for species that show a decrease (left panel) and increase in column density relative to the outflow (right panel) of more than an order of magnitude at any time in the disc chemical model. Different markers and colours show the ratio at different times for the disc model. The shaded regions group species originating from different types of chemistry. Blue: midplane (cosmic ray) chemistry, orange: outer edge (photo) chemistry, dark orange: hot inner edge. Boldfaced labels denote species that are formed via cosmic ray and photochemistry.

Table C1. Parent species and their initial abundances relative to H2 for the disc and outflow chemical kinetics models. Abundances are derived from observations, as compiled by Agúndez et al. (2020).

Species	Initial abundance
He	0.17
CO	3.00×10^{-4}
H_2O	2.15×10^{-4}
N_2	4.00×10^{-5}
SiO	2.71×10^{-5}
H_2S	1.75×10^{-5}
SO_2	3.72×10^{-6}
SO	3.06×10^{-6}
SiS	9.53×10^{-7}
NH_3	6.25×10^{-7}
CO_2	3.00×10^{-7}
HCN	2.59×10^{-7}
PO	7.75×10^{-8}
CS	5.57×10^{-8}
PN	1.50×10^{-8}
HCl	1.00×10^{-8}
HF	1.00×10^{-8}
Cl	1.00×10^{-8}
Mg	1.00×10^{-8}
Fe	1.00×10^{-8}

This paper has been typeset from a TEX/LATEX file prepared by the author.